

Structural and Vibrational Investigation of Römerite,
 $\text{Fe}^{2+}\text{Fe}^{3+}_2(\text{SO}_4)_4 \cdot 14\text{H}_2\text{O}$, under Icy Satellite and Martian
Temperature Conditions

Thesis by
Nina G. Gilkyson

Advisor:
M. Darby Dyar
Department of Astronomy, Mount Holyoke College

MOUNT HOLYOKE COLLEGE
South Hadley, Massachusetts

2022
Defended May 5, 2022

ACKNOWLEDGEMENTS

I would like to extend my everlasting gratitude to Darby Dyar for deciding only eight months ago to mentor a student she had never met before. It is difficult to communicate the impact she and this project has had on my future in academia, and it is also difficult to imagine not working with Darby for many more years. I only wish I had met her earlier.

Likewise, I want to thank Jennifer Jackson for introducing me to the vast world of spectroscopy and to our little mineral, r merite. Last summer, Professor Jackson served as extraordinary and supportive mentor as I dipped my feet into this monster of a project. In doing so, she provided me with valuable opportunities, and I am forever grateful.

Of course, I must thank Olivia Pardo. This project would not have been possible without the countless hours she spent helping me to navigate through its hardest moments. I am happy to call her a mentor and a friend.

I would also like to thank Eli Sklute for contributing many hours out of her full schedule to help and guide me through this project, large aspects of which would not exist without her aid.

I would like to thank Michael Takase at Caltech's X-ray Diffraction Facility, Zhenxian Liu at Brookhaven National Laboratory, George Rossman at Caltech, as well as Tom Tague and Peng Wang at Bruker Optics for their help executing this project.

My home for the last four years has existed within the physics department. It will be difficult to leave all of the amazing professors, staff, and students who kept me

afloat. I would especially like to thank Kerstin Nordstrom for opening the world of research to me and Alexi Arango for his years of guidance.

This work was supported in part by NSF award number 1819209 as well as the Carl F. Braun Trust.

I would like to thank my girlfriend, Madison, for enduring the last eight months of watching me complete this project and supporting me when it got difficult. Finally, I would like to thank my incredible parents (and Smokey), who likewise endured the chaos with a smile. I love you dearly.

ABSTRACT

In the ongoing study of planetary and satellite compositions, spectral data collected from planetary surfaces are often compared to laboratory spectra of minerals collected under Earth's atmospheric conditions. However, temperature can have a significant effect on the underlying physical phenomena that give rise to the spectral features of a mineral. Here, the mixed valence hydrous sulfate r merite, $\text{Fe}^{2+}\text{Fe}_2^{3+}(\text{SO}_4)_4 \cdot 14 \text{H}_2\text{O}$ is used to study these effects. In their investigations of Jupiter's icy satellites, researchers have proposed hydrous sulfates may be a principal constituent of their surfaces, and on Mars, hydrous sulfates have been identified. Thus, these discoveries necessitate a thorough analysis of hydrous sulfates under temperature conditions relevant to these planetary bodies.

Here, single crystal X-ray diffraction, Fourier-transform infrared spectroscopy, Raman spectroscopy, and M ssbauer spectroscopy are used to characterize r merite under low-temperature conditions relevant to icy satellites and Mars. Single crystal X-ray diffraction measurements were taken at temperatures ranging from 100-300K, including a reverse temperature series. The evolution of r merite's unit cell parameters, atomic positions, and bond properties with temperature was observed. Low-temperature Fourier-transform infrared spectroscopy measurements were performed ranging from 20-300K. These results are compared with other hydrous sulfate phases. Complementary to infrared spectroscopy data, Raman spectroscopy data were collected over a temperature range from 153-296K. Approximate band assignments for infrared and Raman spectra are made, and changes in band width, position, and intensity with temperature are discussed. We observe a strong rela-

tionship between temperature and the distortion of water in the structure of römerite, which is evaluated through changes in band width and peak position with temperature. Mössbauer measurements were collected from 4-295K and are still under review, but room temperature Mössbauer measurements of römerite are included in this study. Strong displays of temperature dependence in spectra and data from multiple methods confirms that when performing laboratory comparisons of hydrous sulfates to planetary spectra, temperature-relevant laboratory data should be used to optimize accuracy. The distortion of water molecules in the römerite structure also highlights the importance of studying all hydrous minerals at temperature conditions relevant to planetary bodies of interest.

TABLE OF CONTENTS

Acknowledgements	ii
Abstract	iv
Table of Contents	vi
List of Figures	vii
List of Tables	x
Chapter I: Introduction	1
Chapter II: Background	5
2.1 Hydrrous Sulfates	5
2.2 Römerite	8
2.3 Single Crystal X-ray Diffraction	13
2.4 Molecular Spectroscopy Methods	17
2.5 Mössbauer Spectroscopy	28
Chapter III: Methods	35
3.1 Römerite Sample Preparation	35
3.2 Single Crystal X-ray Diffraction	36
3.3 Fourier-Transform Infrared Spectroscopy	40
3.4 Raman Spectroscopy	40
3.5 Mössbauer Spectroscopy	41
Chapter IV: Results	42
4.1 X-ray Diffraction	42
4.2 Fourier-Transform Infrared Spectroscopy	47
4.3 Raman Spectroscopy	51
4.4 Mössbauer Spectroscopy	52
Chapter V: Discussion	56
Chapter VI: Conclusion	61
Bibliography	64

LIST OF FIGURES

<i>Number</i>	<i>Page</i>
2.1 Temperature-Pressure graph of Martian and icy satellite conditions [Hussmann et al., 2015; Pardo et al., 2022].	9
2.2 Structure of römerite. Two SO ₄ tetrahedra are linked by an Fe ³⁺ octahedron [Dyar et al., 2013].	10
2.3 An example of a single unit cell [Waseda et al., 2011].	13
2.4 Examples of Miller index representation [Waseda et al., 2011].	14
2.5 Simplified schematic of X-ray diffraction by planes of atoms in a crystal. Image adapted from Krane (2012).	15
2.6 Simplified representation of the many different atomic planes in a crystal that can diffract X-rays [Krane, 2012].	16
2.7 Simplified illustration of how a Laue pattern is collected. Image adapted from Krane (2012).	17
2.8 Simplified illustration of (a) the harmonic potential energy model and (b) how it compares to the anharmonic potential energy model (Morse function). x_e is the equilibrium interatomic distance. Image adapted from Pasquini (2003).	21
2.9 Vibrational modes of H ₂ O. The arrows indicate displacement of atoms. ν_1 represents the symmetric stretching vibration, ν_2 represents the bending vibration, and ν_3 represents the asymmetric stretching vibration [Siebert and Hildebrandt, 2008].	23

2.10	Demonstration of the Fourier-transform of an interferogram to produce the final spectrum as a function of wavenumber. Image adapted from Markovich et al. (1991).	24
2.11	Idealized model of inelastic (Stokes and anti-Stokes) and elastic (Rayleigh) scattering of photons. Recall a photon's energy is expressed as $E_p = h\nu$. Image adapted from Siebert et al. (2008).	27
2.12	Simplified representation of nuclear resonant absorption. (a) The source nucleus, in an excited state with a lifetime τ , will decay and emit a gamma ray. (b) The energy of the gamma photon follows a Lorentzian distribution. (c) The emitted gamma ray encounters another identical atom, where it is absorbed and reemitted [Dyar et al., 2006].	30
2.13	(a) Three examples of Mössbauer transmission spectra, illustrating isomer shift, quadrupole splitting, and hyperfine splitting. Relative velocity refers to the velocity of the source nucleus relative to the sample. This movement will Doppler shift the energy spectrum of the emitted gamma ray. At each velocity value, the percent transmission is determined by the amount the emitted gamma spectrum overlaps with the spectrum of the absorber nucleus. (b) Isomer shift, quadrupole splitting, and hyperfine splitting shown using the energy levels of the nucleus. $\pm 1/2$ and $\pm 3/2$ represent the intrinsic angular momentum of the nucleus, or the nuclear spin [Dyar et al., 2006].	32
3.1	Sample CIT-15681 from the Caltech Mineral Collection	35

3.2	Sample CIT-15681-B before being cleaned of trace amounts of halotrichite and an unknown black mineral.	36
4.1	Crystal structure of römerite at three different orientations.	43
4.2	Temperature dependence of römerite's lattice parameters a , b , c and lattice angles α , β , and γ	44
4.3	Temperature dependence of römerite's unit cell volume	45
4.4	Comparison of the volume temperature dependence of römerite, other hydrous sulfates [Talla and Wildner, 2019; Comodi et al., 2017], the silicate bridgmanite [Ross and Hazen, 1989], and the hydroxide boehmite [Berar et al., 1984].	46
4.5	Temperature dependence of a select few S–O and Fe–O bond lengths and S–O–Fe bond angles.	47
4.6	Infrared spectra from 20-300K, separated into three relevant regions. Each region has its own intensity scale. Thus, inter-regional intensity comparisons should not be made. The 297K spectrum was taken before the sample was cooled to 20K and reheated to 300K.	48
4.7	Temperature dependence of a select few bands corresponding to the first fundamental vibration of H ₂ O. Refer to Table 4.1 for more information about band assignments.	50
4.8	Raman spectra from 150-300K, separated into four relevant regions. Each region has its own intensity scale. Thus, inter-regional intensity comparisons should not be made. The 296K* spectrum was taken before the sample was cooled to 153K and reheated to 293K.	52
4.9	Mössbauer transmission spectrum of römerite at 295K.	55

LIST OF TABLES

<i>Number</i>	<i>Page</i>
2.1 Chemical formulas of minerals relevant to this thesis.	6
2.2 Lattice Parameters of Römerite	12
2.3 The Seven Crystal Systems [Waseda et al., 2011]	14
3.1 XRD fit quality data for the reverse temperature series.	37
3.2 XRD fit quality data for the forward temperature series.	38
3.3 XRD fit quality data for the forward temperature series: continued.	39
4.1 Approximate band assignments of römerite's infrared spectrum at 20K.	49
4.2 Approximate band assignments of römerite's Raman spectrum at 20K.	53
4.3 Mössbauer parameters of römerite. The parameters δ and Δ are expressed in mm/s units.	54

Chapter 1

INTRODUCTION

As humanity finds itself on the precipice of groundbreaking missions to space, there are countless ways in which scientists find themselves preparing. The international field of space exploration is split into numerous subfields, each essential and intriguing in its own way. This thesis is just one example of such a worldwide effort.

To understand the big picture of the geophysical, hydrological, atmospheric, and biological aspects of a planetary body, much of the fundamental research occurs on Earth. In the field of mineralogy, this includes researching hundreds of minerals, their relevance to conditions known to be present on planetary bodies of interest, and how they behave under these conditions. Even the knowledge of just a few minerals may provide tremendous insight into larger planetary processes of change, including, but certainly not limited to, ocean circulation, volcanic eruptions, and hydrothermal activity. Equipped with this knowledge, more questions arise, promoting a lively cycle of scientific research.

Mars was first discovered in 1610 by Galileo Galilei, and in what seems like a retrospectively short amount of time, Viking 1 landed on Mars in 1976. Since then, and with the tremendous help from several rovers and other landers, an arsenal of information about the Red Planet's composition and evolution has been generated. This information has led mineralogists on a long and sometimes perilous journey, researching not simply the minerals on Mars, but also refining how these minerals are studied in general.

There is comparatively less information about the mysterious icy bodies in our solar system. Some of the most prominent (research-wise) of these icy satellites includes Jupiter's moons Europa, Ganymede, and Callisto as well Saturn's moon Enceladus. As of now, data from various remote sensing methods have informed guesses about the compositions of icy satellite surfaces. These observations coupled with laboratory research have led to tremendous new insights, and motivated the development of the Europa Clipper mission to further the investigation.

The quest to understand the mineral phases present on other planetary bodies branches forth from a tangled web of many different timelines. However, one of the most important takes root in the 1800s and extends to the present day. During this time, many brilliant physicists, chemists, and biologists grappled with how different regions of the electromagnetic spectrum could be used to accurately probe new and unexplored territories. This exploration of energy came with a lethal price for some, but their work resulted in breakthrough discoveries of the physical world that surrounds us. It also opened up new methods of studying materials that are absolutely essential to the field of space exploration. The basic theory behind these methods, including X-ray diffraction, infrared spectroscopy, Raman spectroscopy, and Mössbauer spectroscopy is discussed in this paper.

This project investigates the mineral römerite, $\text{Fe}^{2+}\text{Fe}^{3+}_2(\text{SO}_4)_4 \cdot 14\text{H}_2\text{O}$. Following its discovery, römerite has been the sole subject of several studies and has also been included in broader investigations of iron sulfate minerals. There remains, however, no thorough investigation of römerite using a variety of analytical methods under different temperature conditions. Römerite, while not confirmed to exist on Mars or any icy satellite, belongs to a group of minerals that scientists believe to be present

on many planetary bodies: hydrous sulfates. On Earth, however, römerite is found around the world, particularly in acid mine drainages in sulfur rich localities [Jambor et al., 2000].

Today, mineralogists and planetary scientists continue to collect spectral data of a tremendous array of minerals, including hydrous sulfates. These data are used to compare to remote spectroscopy data collected on or above the surfaces of other planetary bodies. While this comparison has strengthened our understanding of planetary compositions, much of the spectral data taken on Earth are acquired under Earth's atmospheric temperature and pressure conditions. We know, however, that the ambient temperatures on Mars and icy satellites differ significantly from Earth, and the effects of these two factors on a spectrum cannot be ignored without the risk of misunderstandings and misidentifications. With this in mind, research of minerals relevant to planetary bodies is increasingly done under the appropriate atmospheric conditions, as is done in this thesis.

Upon decreasing the temperature of a solid sample to reflect planetary conditions, it is expected that some structural distortion will occur, albeit on a very small scale. Such microscopic changes in the internal structure and symmetry of the crystal lattice often manifest as large changes in their molecular and nuclear vibrations, which are observed in this thesis using three different spectroscopy methods: infrared, Raman, and Mössbauer. Evaluating these analytical techniques, along with a thorough image of römerite's crystal structure provided by X-ray diffraction measurements, uncovers any isochemical changes or structural phase transitions that occur at low temperatures. This information not only improves reference spectra available for planetary scientists, but provides valuable insights into how hydrous minerals as a

whole respond to different temperature conditions. Because they contain both water and sulfur in their structure, römerite and its associated group of minerals could play an interesting part in the water cycle and sulfur cycle, respectively, on Mars and icy satellites. On a broader scale, research of these processes can reveal key information about the evolution of planetary bodies, our solar system, and the potential for life sometime in the past, present, or future.

Chapter 2

BACKGROUND

2.1 Hydrous Sulfates

Sulfates are a class of minerals containing the sulfate anion $(\text{SO}_4)^{2-}$, which most commonly forms ionic bonds with metals [Richards, 1998]. In sulfate minerals, oxidized sulfur occurs in the S^{6+} valence state. Thus, it has six valence electrons available for bonding and will form covalent bonds with four oxygen atoms, creating the tetrahedral sulfate anion [Hawthorne et al., 2000]. All sulfate minerals can be split into anhydrous and hydrous categories, the latter of which is the focus of this thesis.

Hydrous sulfates contain the functional group H_2O in their structure. Simple hydrous sulfates with divalent cations (M) are of the form $M^{2+}\text{SO}_4 \cdot n\text{H}_2\text{O}$. Possible divalent cations include Zn^{2+} , Mg^{2+} , and Fe^{2+} . These divalent hydrous sulfates can alter to mixed divalent-trivalent sulfates, many of which are of the form $AR(\text{SO}_4)_x \cdot n\text{H}_2\text{O}$, where A is Mg , Fe^{2+} , Mn^{2+} , Co^{2+} , or Zn , and R is Al , Fe^{3+} , or Cr^{3+} [Jambor et al., 2000].

Hydrous Sulfates on Earth

On Earth, the weathering and oxidation of sulfide minerals, including pyrite, chalcopyrite, pyrrhotite, and marcasite (Table 2.1), lead to the formation of hydrous sulfates [Dyar and Gunter, 2008]. Sulfide minerals in metal and coal mines interact with water in acid mine drainages, creating low pH environments that pose

Table 2.1: Chemical formulas of minerals relevant to this thesis.

Name	Chemical Formula
Alunogen	$\text{Al}_2(\text{SO}_4)_3 \cdot 17\text{H}_2\text{O}$
Bilinite	$\text{Fe}^{2+}\text{Fe}^{3+}_2(\text{SO}_4)_4 \cdot 22\text{H}_2\text{O}$
Blödite	$\text{Na}_2\text{Mg}(\text{SO}_4)_2 \cdot 4\text{H}_2\text{O}$
Boehmite	$\text{AlO}(\text{OH})$
Bridgmanite	MgSiO_3
Chalcopyrite	CuFeS_2
Copiapite	$\text{Fe}^{2+}\text{Fe}^{3+}_4(\text{SO}_4)_6(\text{OH})_2 \cdot 20\text{H}_2\text{O}$
Coquimbite	$\text{Fe}_2^{3+}(\text{SO}_4)_3 \cdot 9\text{H}_2\text{O}$
Epsomite	$\text{MgSO}_4 \cdot 7\text{H}_2\text{O}$
Halotrichite	$\text{FeAl}_2(\text{SO}_4)_4 \cdot 22\text{H}_2\text{O}$
Halotrichite	$\text{FeAl}_2(\text{SO}_4)_4 \cdot 22\text{H}_2\text{O}$
Jarosite	$\text{KFe}_3(\text{SO}_4)_2(\text{OH})_6$
Kieserite	$\text{MgSO}_4 \cdot \text{H}_2\text{O}$
Marcasite	FeS_2
Melanterite	$\text{Fe}^{2+}(\text{H}_2\text{O})_6\text{SO}_4 \cdot \text{H}_2\text{O}$
Pyrite	FeS_2
Pyrrhotite	$\text{Fe}_{(1-x)}\text{S}$, where $(x = 0 - 0.2)$
Rhombochase	$(\text{H}_5\text{O}_2)\text{Fe}^{3+}(\text{SO}_4)_2 \cdot 2\text{H}_2\text{O}$
Römerite	$\text{Fe}^{2+}\text{Fe}^{3+}_2(\text{SO}_4)_4 \cdot 14\text{H}_2\text{O}$
Rozenite	$\text{FeSO}_4 \cdot 4\text{H}_2\text{O}$
Siderotil	$\text{FeSO}_4 \cdot 5\text{H}_2\text{O}$
Szomolnokite	$\text{FeSO}_4 \cdot \text{H}_2\text{O}$
Voltaite	$\text{K}_2\text{Fe}^{2+}_5\text{Fe}^{3+}_3\text{Al}(\text{SO}_4)_{12} \cdot 18\text{H}_2\text{O}$

numerous health risks to the local ecosystem. From these contaminated waters, hydrous sulfates often precipitate. Iron-containing hydrous sulfates, in particular, tend to form from the oxidation of iron sulfides, such as pyrite [Jambor et al., 2000; Yen et al., 2008; Dyar and Gunter, 2008; Hurowitz et al., 2009]. Notable iron-containing hydrous sulfates include szomolnokite, römerite, bilinite, siderotil, melanterite, and rozenite.

Hydrous Sulfates on Mars

Analysis of data from the Mars Exploration Rovers (MERs) Spirit and Opportunity, the Mars Express European Space Agency (ESA), and the Mars Reconnaissance Orbiter (MRO) missions has identified sulfate minerals on the Martian surface [Hurowitz et al., 2009]. Hydrous sulfates like kieserite, copiapite, epsomite, and halotrichite were possibly identified using data from the visible and infrared imaging spectrometer OMEGA on board the Mars Express mission [Gendrin et al., 2005; Bibring et al., 2005]. Furthermore, Mössbauer spectrometers on both Mars rovers have identified several iron-bearing minerals, including hematite and the hydrous sulfate jarosite [Klingelhofer et al., 2006]. Magnesium sulfates were also found [Squyres et al., 2005].

Martian temperatures range from 90-300K [Talla and Wildner, 2019]. Acidic conditions and low temperatures in Martian permafrost may provide an appropriate environment for sulfates to form [Dyar et al., 2013]. It is also possible that iron sulfates precipitated from sulfur-rich hydrothermal fluids and volcanic gasses that rapidly cooled and condensed on the surface of the planet [Yen et al., 2008].

Hydrous Sulfates on Icy Satellites

NASA's Galileo mission to Jupiter was prolific in studying its moon Europa, and the Near Infrared Mapping Spectrometer (NIMS) on board the spacecraft performed over 70 observations of its surface [J. Dalton et al., 2012]. To determine Europa's surface composition, NIMS reflectance data have been compared to linear mixtures of laboratory spectra. Early analysis indicated the presence of abundant water ice in the high-albedo regions of the moon and hydrated minerals in the lower-albedo

regions. Of this group of minerals, hydrous sulfates and hydrated carbonates are considered to be the best match [McCord et al., 1998]. In particular, hydrated sodium and magnesium sulfates have been proposed as principle non-ice components of Europa's surface [J. B. Dalton, 2007]. Sulfuric acid hydrate is also considered as a possible component of the satellite surface [Carlson et al., 2009; J. Dalton et al., 2012].

The origins of sulfur present on Europa's surface are debated. Exogenous sources have been proposed, such as the deposition of sulfur ions from Jupiter's magnetosphere [Carlson et al., 2009; Ding et al., 2013]. Endogenic origins are also considered, and sulfur may come to the surface through various surface-interior exchange processes like tectonics, cryovolcanism, and plumes [Carlson et al., 2009; Soderlund et al., 2020]. Regardless of its origins on Europa - whether endogenic, exogenic, or both - sulfur is most likely to exist in the more stable sulfate form because ample oxygen is present to form oxidized minerals [Carlson et al., 2009].

Relevant icy satellite temperature conditions range from 40-300K [Hussmann et al., 2015]. Temperature and pressure conditions for various icy satellites are illustrated in Figure 2.1.

2.2 Römerite

Römerite, $\text{Fe}^{2+}\text{Fe}^{3+}_2(\text{SO}_4)_4 \cdot 14\text{H}_2\text{O}$, was first discovered in the Rammelsberg Mine in Lower Saxony, Germany and identified by Grailich in 1858 [VanLoan and Nuffield, 1959]. Römerite is a mixed valence hydrous sulfate that crystallizes in the triclinic $P\bar{1}$ space group. Its structure consists of Fe^{2+} octahedra coordinated with six H_2O molecules [$\text{Fe}^{2+}(\text{H}_2\text{O})_6$], as well as Fe^{3+} octahedra coordinated with four H_2O

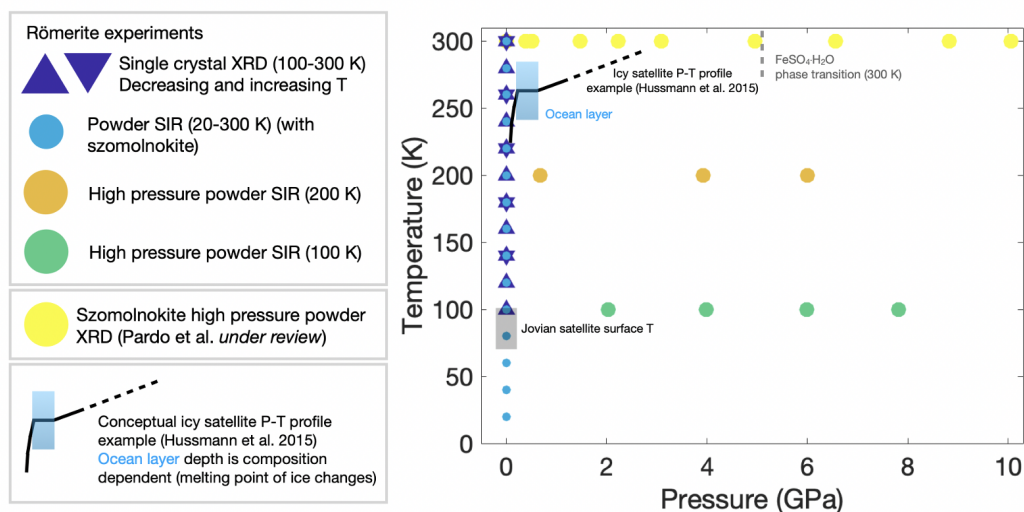


Figure 2.1: Temperature-Pressure graph of Martian and icy satellite conditions [Hussmann et al., 2015; Pardo et al., 2022].

molecules and two oxygen atoms. These oxygen atoms are shared with two sulfate tetrahedra, forming $\text{Fe}^{3+}(\text{SO}_4)_2(\text{H}_2\text{O})_4$ clusters [Fanfani et al., 1970]. A portion of römerite's crystal structure is illustrated in Figure 2.2.

Römerite is a product of the oxidation of iron sulfides, particularly pyrite [Mauro et al., 2019]. On Earth, römerite is associated with the minerals rhomboclase, bilinite, copiapite, jarosite, voltaite, alunogen, and coquimbite (Table 2.1) [Jambor et al., 2000].

Previous Work with Römerite

After römerite's discovery in 1858, Blaas (1884) was the first to perform a crystallographic study of the mineral [Wolfe, 1937]. Through several studies spanning the subsequent 50 years, there was disagreement over the orientation of römerite's crystal axes. This was settled by Wolfe (1937), whose orientation was used in all

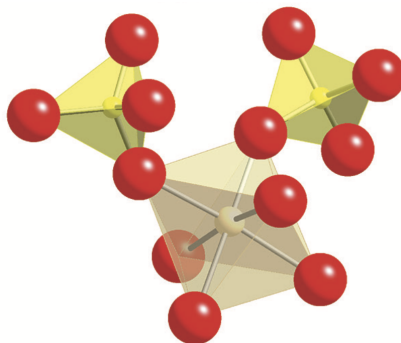


Figure 2.2: Structure of r merite. Two SO_4 tetrahedra are linked by an Fe^{3+} octahedron [Dyar et al., 2013].

further studies of r merite. Van Loan et al. (1959) performed one of the earliest X-ray studies of the mineral using a two-circle reflection goniometer. They report lattice parameter data at atmospheric conditions. Fanfani et al. (1970) went on to make single crystal X-ray diffraction measurements of the mineral, providing lattice parameter and hydrogen bond and angle data. This study became the standard by which all future studies of r merite are compared. Mauro et al. (2019) improved knowledge of r merite's structural arrangement by using a higher-quality single crystal X-ray diffractometer as well as performing micro-Raman measurements. The paper reports lattice parameter, select bond length, and vibrational mode data at atmospheric conditions. Westland (2012) provides another detailed analysis of the crystal structure and bonding environment of r merite in a masters thesis. Lattice parameter data from these studies and others are given in Table 2.2.

To expand the collection of laboratory spectra available to compare to MER M ssbauer data, Dyar et al. (2013) presented an extensive M ssbauer study of iron-bearing hydrous sulfates (including r merite) at ambient conditions. Room temperature and low-temperature (80K) M ssbauer parameters of r merite are reported by

Majzlan et al. (2013). Rothstein et al. (2005) also executed low-temperature (200-280K) Mössbauer measurements of römerite. These are the only known studies of römerite at low temperatures.

Table 2.2: Lattice Parameters of Römerite

Source	a (Å)	b (Å)	c (Å)	α (°)	β (°)	γ (°)	V (Å ³)
Van Loan et al. (1959)	6.48	15.26	6.27	90.07	100.8	85.47	608.8
Fanfani et al (1970)	6.463(8)	15.309(18)	6.341(8)	90.53(17)	101.08(17)	85.73(17)	—
Frost et al. (2011)	6.447(1)	15.317(4)	6.315(2)	90.18(2)	100.92(2)	85.81(2)	616.5(3)
Majzlan et al. (2011)	6.453(1)	15.309(3)	6.322(1)	90.146(8)	100.932(9)	85.86(1)	—
Westland (2012)	6.4274(3)	15.2490(7)	6.3464(3)	89.72	100.79	85.96	609.40
Mauro et al. (2019)	6.4512(6)	15.323(2)	6.3253(6)	90.131(5)	100.9(4)	85.966(4)	612.41(10)
[This Study]	6.452(2)	15.316(4)	6.319(3)	90.16(2)	100.95(2)	85.84(2)	611.3(7)

2.3 Single Crystal X-ray Diffraction

Shortly after the discovery of X-rays in 1895, German physicist Max von Laue discovered the atomic spacing of crystals is appropriate for diffracting X-rays [Perles, 2020; Waseda et al., 2011]. His work gave rise to a common and powerful method of studying the structure of crystals at the atomic level.

To understand the use of X-ray diffraction, some fundamental information about crystal structure and classification is necessary. A crystal is a three-dimensional lattice of small, repeated units of atoms, known as a unit cell (Figure 2.3). Unit cells can be defined by the three vectors **a**, **b**, and **c** (or the lengths a , b , c), and the angles between them: α , β , and γ . These lengths and angles are referred to as lattice parameters. Minerals can be distinguished by their crystal system, which depends on the shape of their unit cells [Ameh, 2019; Dyar and Gunter, 2008]. A list of crystal systems and their respective lattice conditions is provided in Table 2.3.

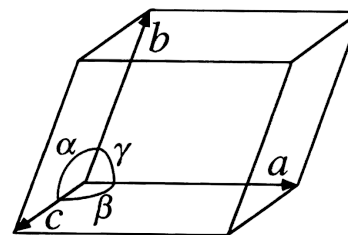


Figure 2.3: An example of a single unit cell [Waseda et al., 2011].

Miller indices are an important coordinate system in crystallography that aid in understanding how atomic planes intersect a crystal's unit cell. Using this system of notation, crystals can be understood as many different parallel planes of atoms, each of which can be represented by the notation (hkl) , with a spacing d_{hkl} between them [Ameh, 2019; Krane, 2012; Waseda et al., 2011].

Table 2.3: The Seven Crystal Systems [Waseda et al., 2011]

Crystal System	Lattice Length Conditions	Lattice Angle Conditions
Triclinic	$a \neq b \neq c$	$\alpha \neq \beta \neq \gamma \neq 90^\circ$
Monoclinic	$a \neq b \neq c$	$\alpha \neq \beta \neq \gamma = 90^\circ$
Orthorhombic	$a \neq b \neq c$	$\alpha = \beta = \gamma = 90^\circ$
Tetragonal	$a = b \neq c$	$\alpha = \beta = \gamma = 90^\circ$
Trigonal	$a = b = c$	$\alpha = \beta = \gamma \neq 90^\circ$
Hexagonal	$a = b \neq c$	$\alpha = \beta = 90^\circ, \gamma = 120^\circ$
Cubic	$a = b = c$	$\alpha = \beta = \gamma = 90^\circ$

h , k , and l for an atomic plane are determined by finding the plane's intercepts with the axes (a , b , c) of the unit cell. If the plane is parallel to an axis, the intercept is infinity. Once the intercepts are found, the reciprocal of the intercepts is taken, giving (hkl) . For example, if a plane intersects the a axis and is parallel to the b and c axes, its Miller index would be written as $\left(\frac{1}{1} \frac{1}{\infty} \frac{1}{\infty}\right)$ or (100) [Waseda et al., 2011; Ameh, 2019]. A number in a Miller index (normally with a magnitude between 1 and 4) represents where the plane cuts the axis [Dyar and Gunter, 2008]. More examples of Miller index representation of crystal planes is shown in Figure 2.4.

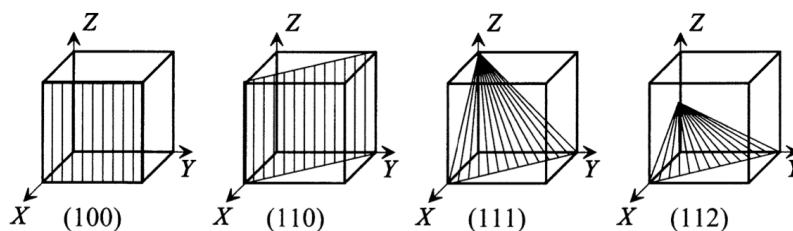


Figure 2.4: Examples of Miller index representation [Waseda et al., 2011].

The wavelength of X-rays ranges from about 10 nm to 10^{-3} nm, while the atomic spacing in a crystal is often around 0.1 nm [Waseda et al., 2011; Krane, 2012]. For X-ray diffraction experiments, wavelengths between 0.05 nm and 0.25 nm are

typically used [Suryanarayana and Norton, 1998].

In order for constructive interference of the diffracted rays to occur, their optical path difference must be $n\lambda$, where $n \in \mathbb{Z}^{\geq 0}$ [Krane, 2012]. Figure 2.5 illustrates a simplified crystal structure comprised of planes of atoms separated by a distance d_{hkl} . The difference between the path length travelled by beam 1 and beam 2 is $2d_{hkl} \sin \theta$. Therefore, according to Bragg's Law, the interference maxima is expressed as

$$n\lambda = 2d_{hkl} \sin \theta.$$

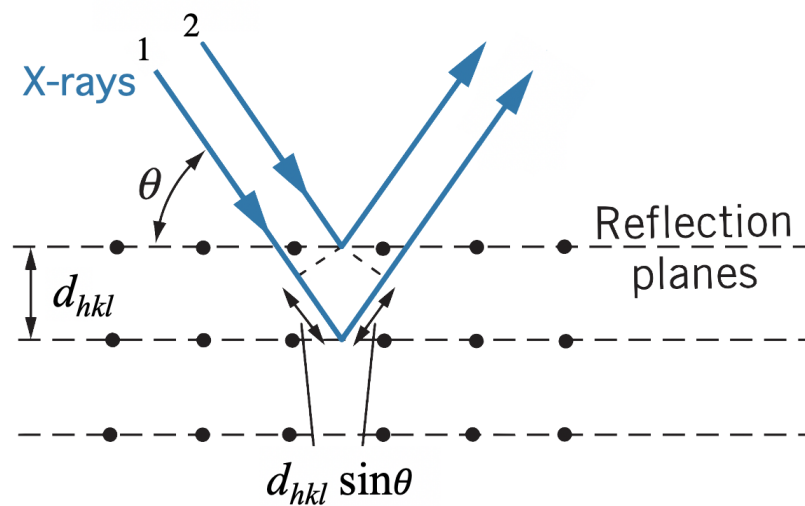


Figure 2.5: Simplified schematic of X-ray diffraction by planes of atoms in a crystal. Image adapted from Krane (2012).

When performing single-crystal X-ray diffraction, the sample is irradiated by a monochromatic beam of X-rays [Waseda et al., 2011]. As illustrated in Figure 2.6, there are many different crystal planes (with different miller indices) that will diffract X-rays, each with a unique interplanar distance and angle of incidence

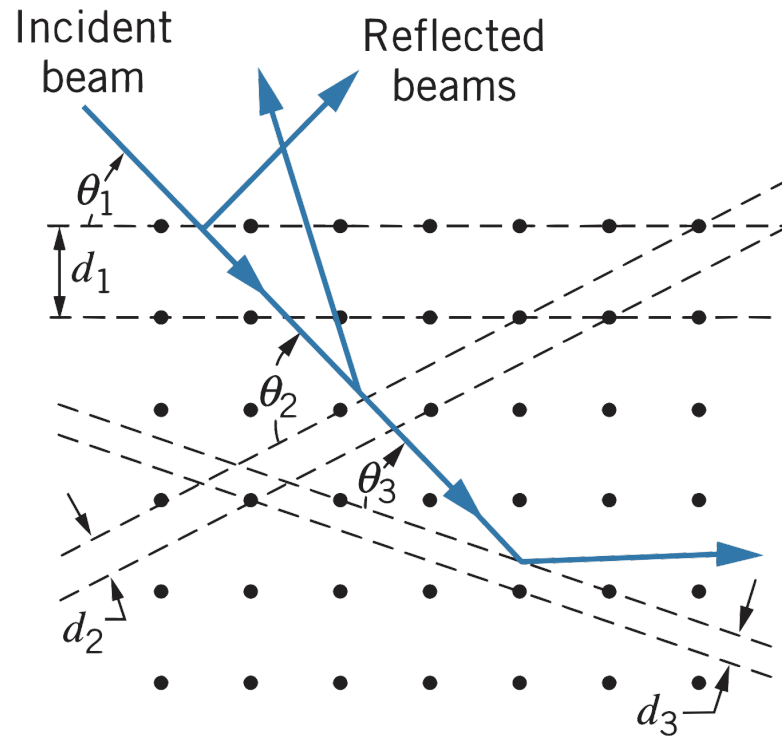


Figure 2.6: Simplified representation of the many different atomic planes in a crystal that can diffract X-rays [Krane, 2012].

corresponding to the incident wavelength. At any single fixed wavelength and one orientation, Bragg's Law is satisfied for only few of the many atomic planes in the single crystal [Krane, 2012]. Thus, the sample is rotated [Waseda et al., 2011]. Constructive interference caused by these different atomic planes creates a diffraction pattern of interference maxima referred to as a Laue pattern [Krane, 2012]. A simplified schematic of creating a Laue pattern is shown in Figure 2.7. Interpreting these patterns reveals the atomic structure of the crystal, its symmetry, the parameters of its unit cell, and its crystal system. This includes information about the sample's bonding environment, allowing observation of how individual

bonds change with temperature.

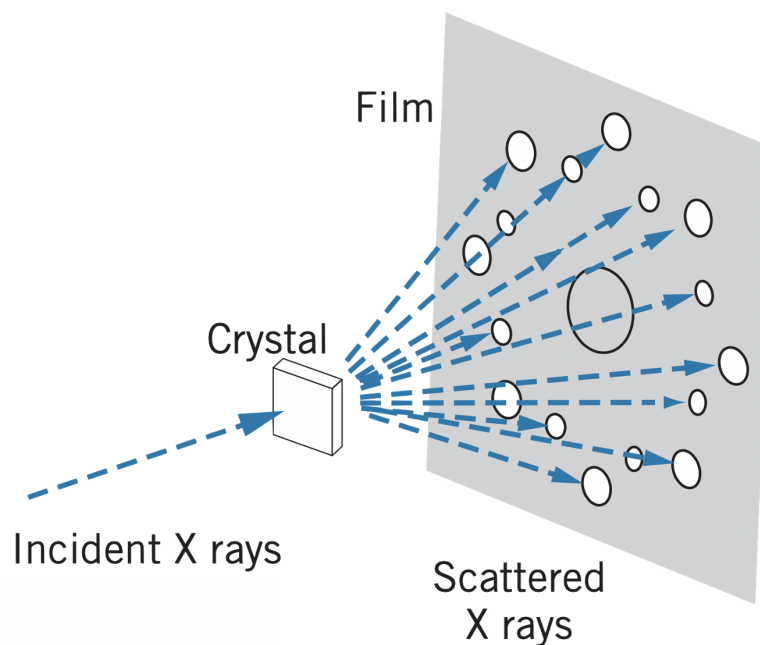


Figure 2.7: Simplified illustration of how a Laue pattern is collected. Image adapted from Krane (2012).

2.4 Molecular Spectroscopy Methods

In this study of r merite, two different, yet complementary, methods of probing the evolution of its molecular structure at different temperatures are employed. Fourier-transform infrared (FTIR) spectroscopy is the first of these methods. This technique relies on molecules absorbing, transmitting, or reflecting light in the infrared (IR) region of the electromagnetic spectrum [Stuart, 2004]. The second method - Raman spectroscopy - results from molecules inelastically scattering light of a higher frequency than IR, often in the visible or UV region [Mitsutake et al., 2019]. Each of these vibrational spectroscopic methods has its own set of

advantages and disadvantages over the other. However, when used together, they provide a thorough image of the molecular properties of a mineral.

Fourier-Transform Infrared Spectroscopy

Infrared light was discovered in the early 1800s by Sir William Herschel, and the first infrared spectrometer was created in 1835 [Theophanides, 2012]. It was not until the 1940s, however, that commercial infrared spectrometers were made available. Since then, infrared spectroscopy has remained a popular analytical method for characterizing a wide range of materials [Stuart, 2004].

Molecules have discrete energy levels, and the differences in energy among these levels corresponds to energies in the infrared region of the electromagnetic spectrum (10^{13} – 10^{14} Hz) [Stuart, 2004]. To excite a molecule from one energy level to another, incident radiation must oscillate with a frequency corresponding to the exact energy difference between the two levels. This relationship is described by

$$\nu = \frac{(E_1 - E_o)}{h}. \quad (2.1)$$

Here, ν is frequency, E_1 is an excited energy state, E_o is a lower energy state (for instance, the ground state), and h is Planck's constant [Stuart, 2004].

These excited vibrational states are unique for every molecule and depend on bond strength and atomic mass. This relationship is illustrated using the simplest case of a diatomic molecule C–D, here treated as a one-dimensional simple harmonic oscillator [Siebert and Hildebrandt, 2008].

According to Hooke's Law, when the atoms in a diatomic molecule are displaced by x , there will be some restoring force

$$F_s = kx, \quad (2.2)$$

where k represents the force constant (or strength) of its only bond. We can express the potential energy, U , of the bond as

$$U = \frac{1}{2}kx^2. \quad (2.3)$$

To simplify the calculations, the reduced mass of the system is expressed as

$$\mu = \frac{m_C \cdot m_D}{m_C + m_D}. \quad (2.4)$$

When Equation 2.3 is plugged into Schrödinger's equation, where $\psi = Ae^{-ax^2}$ (the ground state wavefunction), the ground state E is solved as

$$E = \frac{1}{2}\hbar\sqrt{\frac{k}{\mu}}. \quad (2.5)$$

The general form to this solution is expressed as

$$E_n = \left(n + \frac{1}{2}\right)\hbar\sqrt{\frac{k}{\mu}}, \quad (2.6)$$

where n is the vibrational quantum number [Krane, 2012; Siebert and Hildebrandt, 2008]. The difference in energy between each consecutive level is $\Delta E = \hbar\sqrt{\frac{k}{\mu}}$. Thus, an incoming photon must be equivalent in energy in order to be absorbed by the molecule. Because a photon's energy, E_p , is proportional to its frequency, then $E_p = h\nu$. Therefore, the absorption frequency necessary to excite the diatomic molecule from one level to the next is given by

$$\nu = \frac{1}{2\pi} \sqrt{\frac{k}{\mu}}. \quad (2.7)$$

Equation 2.7, indicates that increasing the bond strength will also increase the absorption frequency. Moreover, if the reduced mass is increased, the absorption frequency decreases [Siebert and Hildebrandt, 2008].

Most oscillating systems can be treated as harmonic oscillators at small displacements around a minimum in its potential energy. For basic comprehension purposes, it is appropriate to treat molecular vibrations as harmonic oscillations [Krane, 2012]. However, there are several fundamental flaws to this simplification that are addressed by considering an anharmonic (rather than the harmonic) potential energy model. The differences between these two models are illustrated in Figure 2.8. The anharmonic potential energy curve, referred to as the Morse function, considers the repulsion force between two atoms as they closely approach each other and the dissociation resulting from a very large interatomic distance. The energy levels of the anharmonic potential model are not equally spaced as they are for the harmonic model, rather they condense at higher quantum numbers [Pasquini, 2003].

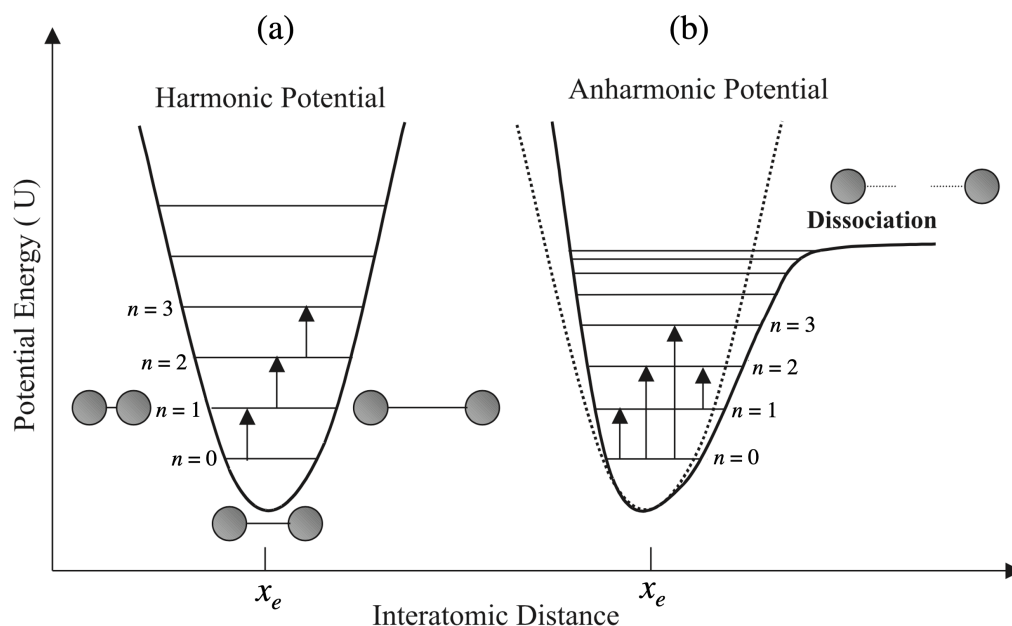


Figure 2.8: Simplified illustration of (a) the harmonic potential energy model and (b) how it compares to the anharmonic potential energy model (Morse function). x_e is the equilibrium interatomic distance. Image adapted from Pasquini (2003).

The harmonic model dictates that energy transitions can only be made one level at a time. This is not what is observed in spectral data, however. According to the anharmonic model, transitions that span two or more energy levels are also possible [Pasquini, 2003]. These manifest on a spectrum as overtones. Fundamental vibrations are transitions from the ground state to the first excited state. For a diatomic molecule, this is its stretching mode. The first overtone band occurs when a molecule transitions from the ground to the second excited energy state. Its energy can be estimated by doubling the energy of the fundamental vibration [Pasquini, 2003; Stuart, 2004]. The second overtone occurs when when the vibrational energy of the molecule is excited from the ground to the third excited state, and so on.

Fundamental transitions are most likely to occur and the probability of observing overtones in a spectrum decreases significantly as the number of levels transitioned increases [Stuart, 2004].

Previously, the potential energy of the bond in a diatomic model was expressed as

$$U = \frac{1}{2}kx^2.$$

However, in considering anharmonicity, the full Taylor series expansion about the minimum x_e of a diatomic molecule's potential energy must be examined:

$$U(x) = U(x_e) + \left(\frac{\partial U}{\partial x}\right)_{x_e} (x - x_e) + \frac{1}{2!} \left(\frac{\partial^2 U}{\partial x^2}\right)_{x_e} (x - x_e)^2 + \frac{1}{3!} \left(\frac{\partial^3 U}{\partial x^3}\right)_{x_e} (x - x_e)^3 + \dots$$

The first three terms of this expansion suffice for describing a harmonic oscillator. In considering the cubic term, however, the anharmonicity of a molecule's potential energy is addressed, as is the temperature dependence of band width and position [Nesbitt et al., 2018; Balkanski et al., 1983].

The earlier explanation of the harmonic and anharmonic potential models considers only a simple diatomic molecule, which has one fundamental mode of vibration. However, the number of modes for a more complex, non-linear polyatomic molecule is given by $3N - 6$, where N is the number of atoms in the molecule. For a triatomic molecule, these vibrational modes consist of two stretching modes - symmetric and antisymmetric - and one bending mode [Stuart, 2004]. A common and relevant example of a triatomic molecule is H_2O , and its associated vibrations are illustrated

in Figure 2.9. A fundamental mode is considered infrared-active if it experiences a change in the permanent dipole moment of the molecule when vibrating. Otherwise, the molecule will not absorb infrared radiation, and no absorption peaks will be observed in the final spectrum [Stuart, 2004]. All three fundamental modes of H₂O are IR-active [Vandenabeele, 2013].

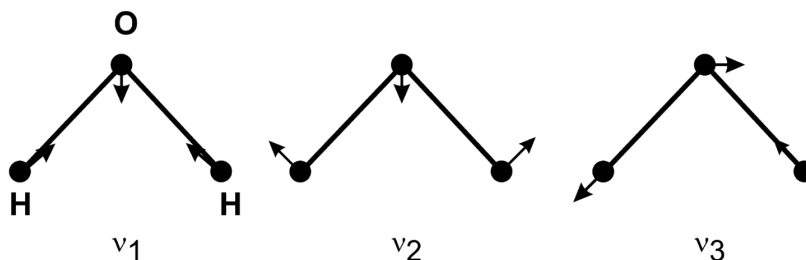


Figure 2.9: Vibrational modes of H₂O. The arrows indicate displacement of atoms. ν_1 represents the symmetric stretching vibration, ν_2 represents the bending vibration, and ν_3 represents the asymmetric stretching vibration [Siebert and Hildebrandt, 2008].

The invention of Fourier-transform infrared spectrometers considerably increased the accuracy, speed, and popularity of IR spectroscopy. This method uses an interferometer to create a signal (or an interferogram) that is a function of the optical path difference (OPD) between two beams. First, a beam of polychromatic infrared light is split in two by a beamsplitter. These two beams travel to perpendicular mirrors, a stationary mirror and a moving mirror, where they will reflect and return to the beamsplitter. Depending on the position of the moving mirror, the two beams will interfere either constructively or destructively. For an OPD of $(n + \frac{1}{2})\lambda$ where $n \in \mathbb{Z}^{\geq 0}$, the two beams will destructively interfere, and for an OPD of $n\lambda$, the beams will constructively interfere. The interference pattern for a polychromatic source is shown in Figure 2.10, with the maximum occurring when the OPD is 0. The signal

from the interferometer is sent to the sample and picked up by the detector [Stuart, 2004].

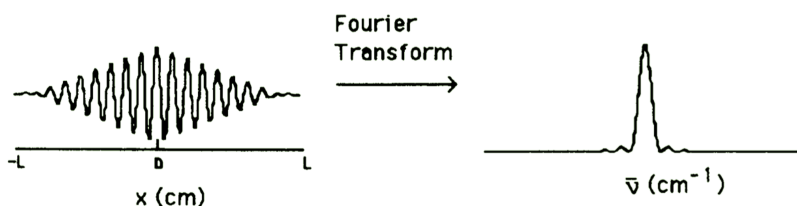


Figure 2.10: Demonstration of the Fourier-transform of an interferogram to produce the final spectrum as a function of wavenumber. Image adapted from Markovich et al. (1991).

Taking the Fourier transformation of the signal after passing through the sample produces a signal that is a function of wavenumber (which is proportional to energy). This is the desired infrared spectrum [Stuart, 2004].

Raman Spectroscopy

The Raman effect, also known as Raman scattering, was theorized by Adolf Smekal in 1923 [Mitsutake et al., 2019]. It was proven several years later by C. V. Raman and K. S. Krishnan, who demonstrated the inelastic scattering of light by a liquid. Methods used by Raman and Krishnan to collect early spectra significantly advanced with the invention of lasers in the 1960s. From then on, Raman spectroscopy became an increasingly popular analytical tool in a variety of fields, including mineralogy [Vandenabeele, 2013].

In comparison to infrared spectroscopy, the Raman effect involves the scattering - rather than the absorption - of photons when they encounter some material [Siebert and Hildebrandt, 2008]. The following discussion of the Raman effect considers the

classical approach outlined by Vandenabeele (2013). In the presence of an external electric field \mathbf{E} , oscillating with a frequency ω_o , a molecule will have an induced dipole moment,

$$\mathbf{p} = \alpha \mathbf{E}_o \cos(\omega_o t). \quad (2.8)$$

Here, α is a second order tensor that represents the polarizability of a molecule. Polarizability measures the ability of a molecule's valence electron cloud to distort and relies on the shape and dimensions of the molecule's chemical bonds [Choudhary et al., 2020; Vandenabeele, 2013]. Thus, the polarizability depends on the normal coordinate (or nuclear displacement), Q , where α is a linear function of Q ,

$$\alpha = \alpha_o + \alpha' Q. \quad (2.9)$$

Here, α' represents the derivative of the polarizability tensor with respect to the normal coordinate under equilibrium conditions.

If a molecule oscillates with a frequency ω_{vib} , the normal coordinate is expressed as

$$Q = Q_o \cos(\omega_{vib} t). \quad (2.10)$$

By combining Equations 2.8, 2.9, and 2.10, the following expression for the induced dipole moment is derived:

$$\mathbf{p} = (\alpha_o + \alpha' Q_o \cos(\omega_{vib}t)) \cdot \mathbf{E}_o(\cos \omega_o t). \quad (2.11)$$

Using the trigonometric property that $\cos A \cos B = \frac{1}{2}[\cos(A + B) + \cos(A - B)]$, Equation 2.11 becomes

$$\mathbf{p} = \alpha_o \mathbf{E}_o \cos(\omega_o t) + \frac{\alpha' \mathbf{E}_o Q_o}{2} \cos[(\omega_o + \omega_{vib})t] + \frac{\alpha' \mathbf{E}_o Q_o}{2} \cos[(\omega_o - \omega_{vib})t]. \quad (2.12)$$

The relationship between the induced dipole moment, the vibrational frequency of the molecule, and the frequency of incident radiation can further simplify to

$$\mathbf{p} = \mathbf{p}(\omega_o) + \mathbf{p}(\omega_o + \omega_{vib}) + \mathbf{p}(\omega_o - \omega_{vib}). \quad (2.13)$$

In Raman spectroscopy, a small part of the sample is irradiated with a laser beam of monochromatic light [Vandenabeele, 2013]. The vast majority of the photons emitted by the Raman spectrometer's laser will be scattered with virtually no change in energy. This is referred to as Rayleigh or elastic scattering. The first component in Equation 2.13, corresponds to this phenomenon; the induced dipole moment oscillates at the same frequency as the incident radiation, ω_o .

The Raman effect involves Stokes and anti-Stokes inelastic scattering, which is illustrated in Figure 2.11. Anti-Stokes scattering is less likely than Stokes scattering to occur at room temperature [Mitsutake et al., 2019]. Here, the energy of the

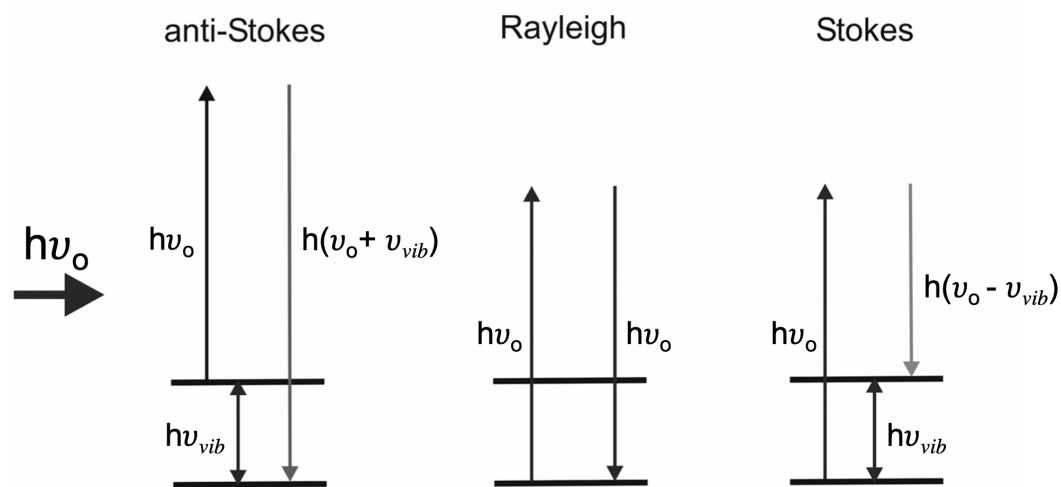


Figure 2.11: Idealized model of inelastic (Stokes and anti-Stokes) and elastic (Rayleigh) scattering of photons. Recall a photon's energy is expressed as $E_p = h\nu$. Image adapted from Siebert et al. (2008).

emitted photon is larger than the energy of the incident photon. This is illustrated by the second term in Equation 2.13. In this case, a molecule that is in an excited vibrational state relaxes to the ground state, and in doing so, transfers the exact energy of that excited vibrational frequency to the emitted photon. The difference in energy between the incident photon and the emitted photon should correspond to the excited vibrational state the molecule occupied before it scattered the photon [Vandenabeele, 2013; Mitsutake et al., 2019].

Stokes scattering, which is the more common of the two, occurs when an emitted photon has less energy than the incident photon. This is illustrated by the third term in Equation 2.13, where $\omega_0 - \omega_{vib}$. In this case, some of the incident photon's energy was used to excite a functional group in the material. The difference between the energies of incident photons and emitted photons should correspond to unique

vibrational modes of molecules in the material [Vandenabeele, 2013; Mitsutake et al., 2019].

If a molecule is Raman-active, there must be a change in its polarizability when the molecule is vibrating. This is in comparison to infrared spectroscopy, where in order to be IR-active, there must be a change in the permanent dipole moment. This distinction is one of the most important selection rules of Raman and IR spectroscopy. In addition to being infrared-active, the three vibrational modes of H₂O are Raman-active. Some molecules like H₂ do not have a permanent dipole and are, therefore, infrared inactive, but Raman-active [Vandenabeele, 2013]. Thus, these two methods are not perfect substitutes of each other, rather complementary in developing a thorough understanding of a mineral's structural properties.

2.5 Mössbauer Spectroscopy

The Mössbauer effect was first discovered in 1957 by Rudolf Ludwig Mössbauer, who received a Nobel Prize for his accomplishment [Yoshida and Langouche, 2013]. Soon after its inception, geoscientists recognized its use in investigating the coordination environments and oxidation states of iron in minerals. Over the last few decades, significant improvements along with the inclusion of Mössbauer spectrometers on the Mars Exploration Rovers (MERS), Spirit and Opportunity, have rendered the technique relevant and in-demand [Dyar et al., 2006].

Mössbauer spectroscopy involves the resonant absorption of gamma rays by a nucleus. Similar to the vibrational modes of a molecule, the atomic nucleus has discrete energy states governed by the principles of quantum mechanics. When the nucleus of an atom relaxes from an excited state to the ground state, it will emit

the transition energy as a gamma photon. The transition energy is not as precisely defined as it is for molecular absorption and emission because the excited nuclear state has a very short, finite lifetime, τ . According to Heisenberg's uncertainty principle, the energy of the nuclear transition thus follows a Lorentzian distribution centered at E_o . The full width half maximum (FWHM) of this distribution or the *natural line width*, Γ_o , is given by

$$\Gamma_o = \frac{\hbar}{\tau}, \quad (2.14)$$

where \hbar is Planck's constant divided by 2π . Likewise, the energy required by the absorber nucleus follows a Lorentzian distribution [Dyar et al., 2006; Dyar and Sklute, 2019].

In an ideal case, a radioactive atom in an excited state E_e will return to the ground state and emit a gamma photon with an energy that follows the Lorentzian distribution. This photon may encounter an atom of the same type, and if the energy distributions for the emitter and absorber nucleus overlap, the absorber nucleus is excited to an energy state E_e . This process, shown in Figure 2.12, continues as the atom returns to ground and emits another photon [Dyar et al., 2006; Dyar and Sklute, 2019].

In reality, however, photons have some momentum, $p_\gamma = E_\gamma/c$, where c is the speed of light and E_γ is the energy of the gamma ray. When a nucleus at rest emits a photon, it will recoil with some momentum $p_{nucleus} = -p_\gamma$, just as a gun recoils when fired. Due to conservation of energy, the energy of this emitted photon will be E_r less than the transition energy, E_o , given by $E_\gamma = E_o - E_r$, where

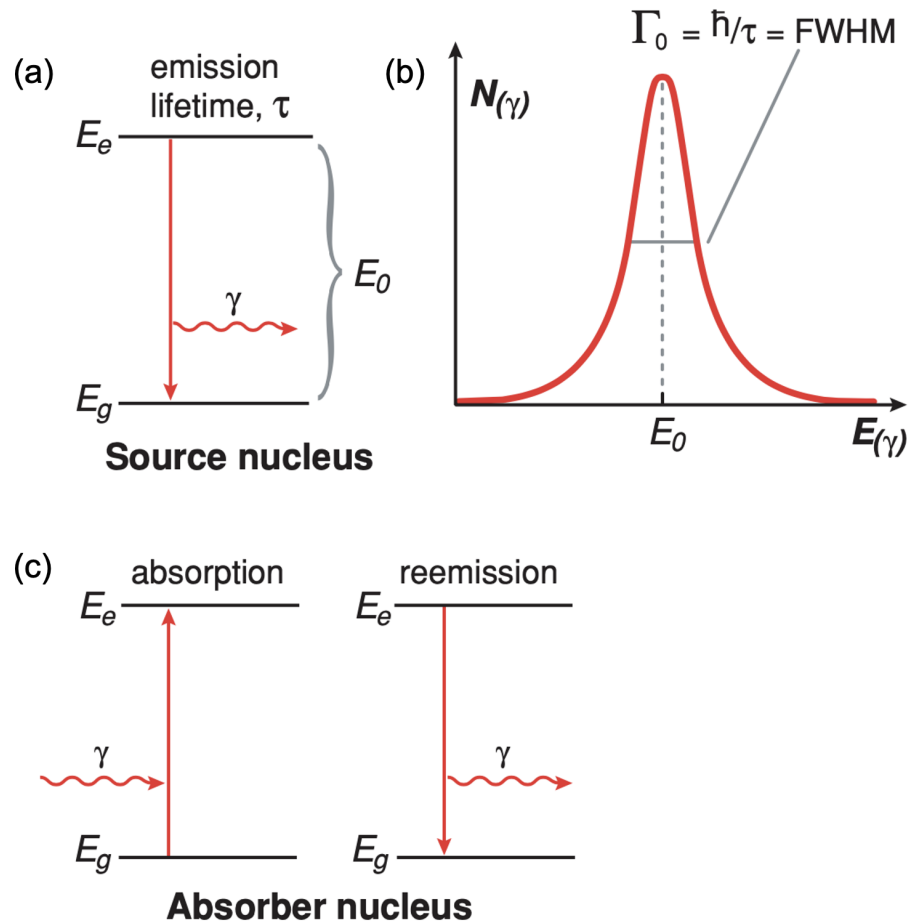


Figure 2.12: Simplified representation of nuclear resonant absorption. (a) The source nucleus, in an excited state with a lifetime τ , will decay and emit a gamma ray. (b) The energy of the gamma photon follows a Lorentzian distribution. (c) The emitted gamma ray encounters another identical atom, where it is absorbed and reemitted [Dyar et al., 2006].

$$E_r = \frac{(p_{nucleus})^2}{2M} = \frac{(-p_\gamma)^2}{2M} = \frac{(E_\gamma)^2}{2Mc^2}. \quad (2.15)$$

Likewise, when a nucleus absorbs a photon, conservation of energy dictates that the energy of the incident photon must be E_r greater than the nuclear transition energy

to account for recoil energy. Therefore, $E_\gamma = E_o + E_r$ [Dyar et al., 2006; Dyar and Sklute, 2019].

The discrepancy in energy between the incident photon and the required transition energy of the absorber nucleus prevents two identical atoms at rest from experiencing nuclear resonant absorption. However, Mössbauer found that if the emitting and absorbing atoms are bound within a crystal lattice, a fraction, f , of nuclear transitions will be recoil-free. This type of transition is referred to as a zero-phonon transition [Dyar et al., 2006; Dyar and Sklute, 2019]. Here,

$$f = 1 - \frac{E_r}{\hbar\omega}, \quad (2.16)$$

where according to the Einstein model, ω is a single frequency corresponding to a vibrational mode of the solid. Ideally $E_r \ll \hbar\omega$. [Dyar et al., 2006; Dyar and Sklute, 2019].

For several reasons, ^{57}Fe is a popular choice for Mössbauer experiments. First, iron is an abundant element on Earth and in the our solar system. Furthermore, ^{57}Fe has a very high fraction of zero-phonon transitions, with an f value ranging from around 0.65 to 1 [Dyar et al., 2006; Dyar and Sklute, 2019].

The energy levels of a nucleus are affected by hyperfine interactions with its local environment. These environmental factors include the number of electrons, the number of coordinating anions, site symmetry, and magnetic ordering. To account for changes in the absorber's transition energy as a result of these hyperfine interactions, the source is oscillated towards and away from the sample with a velocity that

varies linearly with time. Thus, the energy of the emitted gamma ray is Doppler-shifted, accounting for a greater range of possible transmission/absorption values [Dyar et al., 2006; Dyar and Sklute, 2019].

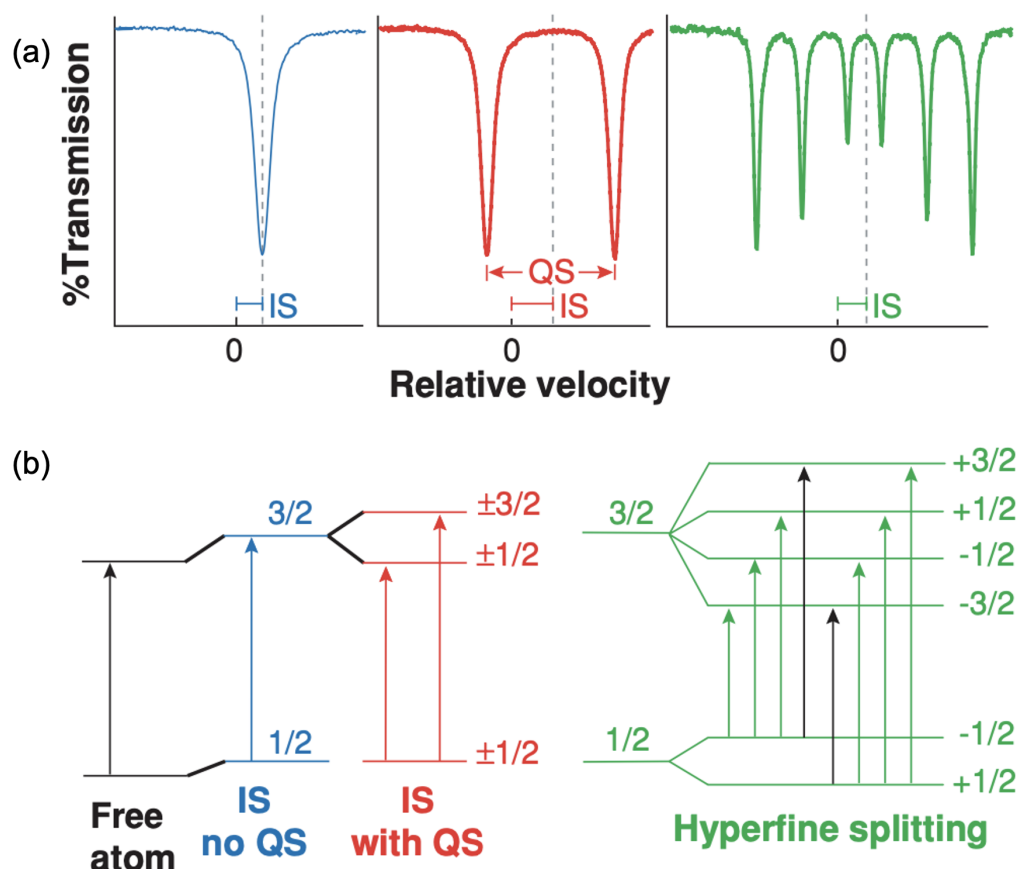


Figure 2.13: (a) Three examples of Mössbauer transmission spectra, illustrating isomer shift, quadrupole splitting, and hyperfine splitting. Relative velocity refers to the velocity of the source nucleus relative to the sample. This movement will Doppler shift the energy spectrum of the emitted gamma ray. At each velocity value, the percent transmission is determined by the amount the emitted gamma spectrum overlaps with the spectrum of the absorber nucleus. (b) Isomer shift, quadrupole splitting, and hyperfine splitting shown using the energy levels of the nucleus. $\pm 1/2$ and $\pm 3/2$ represent the intrinsic angular momentum of the nucleus, or the nuclear spin [Dyar et al., 2006].

If the local nuclear environment of the source atom is different than the absorber atom, there will be a shift in the absorber's transmission spectrum away from zero relative velocity, as seen in Figure 2.13. This is referred to as isomer shift, and corresponds to a difference in the energy levels of the emitter and absorber nucleus. The charge distribution in the nucleus interacts with the electronic charge distribution of the atom. Thus, differences in the electronic charge distribution, or more specifically, differences in the s-electronic charge density between the absorber and emitter atoms, will result in isomer shift, often represented as δ [Dyar et al., 2006; Dyar and Sklute, 2019].

The energy levels of the nucleus are also capable of splitting as a result of the interaction between the quadrupole moment of the nucleus and the electric field gradient at the nucleus (Figure 2.13). If the charge distribution surrounding a nucleus (including the electronic charge distribution of the atom and the charges of the surrounding atoms) is not spherically symmetric, an electric field gradient will exist at the nucleus. The resultant interaction between the quadrupole moment and the electric field gradient will cause the $I = 3/2$ level of nucleus to split into two. This manifests in the Mössbauer spectrum as two peaks, or a doublet. The distance between the two is the quadrupole splitting, QS or Δ [Dyar et al., 2006; Dyar and Sklute, 2019].

If a nucleus with a magnetic moment is exposed to a magnetic field, created either internally or applied externally, then the energy levels of the nucleus will split into six discrete levels (Figure 2.13). On the transmission spectrum, this manifests as a sextet of peaks. This is referred to as magnetic hyperfine splitting, and may occur only at certain temperatures [Dyar et al., 2006; Dyar and Sklute, 2019].

Evaluating isomer shift, quadrupole splitting, and magnetic hyperfine splitting reveals information about the valence state and site occupancy of iron in a mineral. A decrease in isomer shift corresponds to increase in s-electron density, thus making isomer shift responsive to oxidation state and bond lengths and types. In general, isomer shifts values for Fe^{2+} are significantly higher than values for Fe^{3+} . Quadrupole splitting is also sensitive to oxidation state as well as the geometry of the site. Generally, the larger the QS, the more distorted the coordination environment around the Fe is. Furthermore, QS for $\text{Fe}^{2+} \gg$ QS for Fe^{3+} [Dyar et al., 2006; Dyar et al., 2013; Dyar and Sklute, 2019].

Chapter 3

METHODS

3.1 Römerite Sample Preparation

A natural römerite sample was obtained from a larger rock (CIT-15681) consisting of römerite, halotrichite, and an unknown black mineral from the Caltech mineral collection, shown in Figure 3.1.



Figure 3.1: Sample CIT-15681 from the Caltech Mineral Collection

Samples were cleaned of halotrichite and black mineral impurities using a tungsten needle. Before collecting single crystals, a select sample (CIT-15681-B) was washed with ethanol and transferred to a clean petri dish. CIT-15681-B is shown in Figure 3.2. To release fragments, the sample was rolled between two clean glass slides. Fragments approximately 200 μm in length with even edges and flat surfaces were

isolated. Crossed polarizers were used to confirm that selected fragments were single crystals and displayed perfect homogeneous extinction.

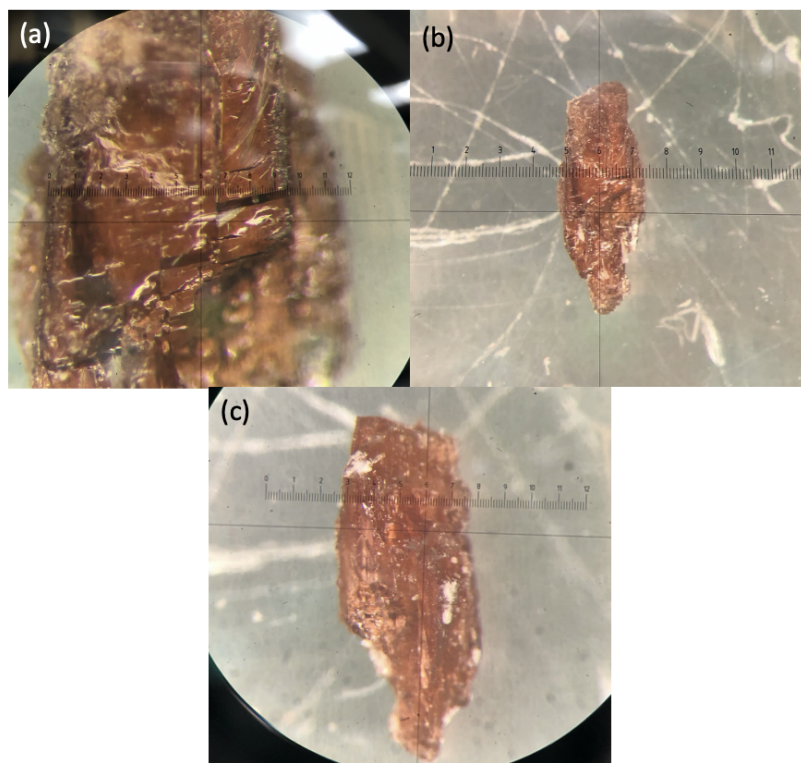


Figure 3.2: Sample CIT-15681-B before being cleaned of trace amounts of halotrichite and an unknown black mineral.

After selecting single crystals, the remaining mineral sample (CIT-15681-B) was ground into a fine powder using a diamonite (iron-free) mortar and pestle. Some additional samples (CIT-15681-C,D,E) were also ground into a fine powder.

3.2 Single Crystal X-ray Diffraction

Lattice parameters were measured by a Bruker D8 single crystal, four-circle diffractometer at the California Institute of Technology's X-ray Crystallography Facility.

The device is equipped with a Oxford Cryosystems nitrogen cooling system and a CMOS detector. Molybdenum radiation from a 2 kW fine focus X-ray tube (0.710737 Å) was used. Before being placed on a Mitigen mount, a small amount of mineral oil was applied to the single crystal. The diffractometer's exposure time was 20 seconds per frame with 1,789 frames at each temperature. Size and quality limitations of the sample restricted the temperature series to 20K intervals for the forward-series, and 40K intervals for the reverse series. Temperature measurements were taken between 100 and 300K.

Diffraction data was integrated in the APEX3 software before being refined in OLEX2-1.3. Römerite's crystal structure was refined at each temperature to an agreement factor $0.030043 \leq R_1 \leq 0.036565$ and a goodness of fit $1.00956 \leq S \leq 1.02128$ on the basis of 2747-2942 reflections ($F_o \geq 4\sigma_F$). More fit information for each temperature in the forward and reverse series is found in Tables 3.1, 3.2, and 3.3.

Table 3.1: XRD fit quality data for the reverse temperature series.

Temperature (K)	140	180	220	260	300
wR_2	0.0675	0.0691	0.0714	0.0764	0.0904
S	1.0199	1.0108	1.0173	1.0169	0.9777
$R_1 [F_o \geq 4\sigma_F]$	0.0310	0.0321	0.0339	0.0357	0.0380
R_1 (all data)	0.0490	0.0520	0.0562	0.0607	0.0674
Reflections with $F_o \geq 4\sigma_F$	2922	2887	2857	2772	2747
Unique Reflections	3660	3668	3683	3686	3705

Table 3.2: XRD fit quality data for the forward temperature series.

Temperature (K)	100	120	140	160	180	200
wR_2	0.0636	0.0661	0.0674	0.0681	0.0704	0.0708
S	1.0190	1.0165	1.0123	1.0155	1.0246	1.0096
$R_1 [F_o \geq 4\sigma_F]$	0.03004	0.03047	0.03156	0.0317	0.03186	0.03283
R_1 (all data)	0.0474	0.0479	0.0488	0.0494	0.0508	0.0523
Reflections with $F_o \geq 4\sigma_F$	2942	2936	2938	2923	2912	2899
Unique Reflections	3662	3662	3659	3664	3673	3675

Table 3.3: XRD fit quality data for the forward temperature series: continued.

Temperature (K)	220	240	260	280	300
wR_2	0.0707	0.0832	0.0780	0.0766	0.0792
S	1.0073	0.9553	1.0309	1.0213	1.0161
R_1 [$F_o \geq 4\sigma_F$]	0.03267	0.03365	0.03551	0.03618	0.03656
R_1 (all data)	0.0536	0.0556	0.0581	0.0606	0.0620
Reflections with $F_o \geq 4\sigma_F$	2861	2848	2851	2804	2776
Unique Reflections	3678	3683	3688	3697	3716

3.3 Fourier-Transform Infrared Spectroscopy

Synchrotron FTIR measurements were performed at Brookhaven National Laboratory, Beamline 22-IR-1. A Bruker Vertex 80v Fourier-Transform Infrared Spectrometer was used. Powder sample of römerite (CIT-15681-B) was loaded on a diamond anvil with a 600 μm culet and a ruby sphere as an in-situ pressure marker. The cryostat was equipped with diamond windows to extend the detectable range of phonon peak frequencies down to 500 cm^{-1} . A spectrum was first collected at room temperature (297K). The temperature of the sample was cooled to 20K before being increased to 300K in increments of 20K. Background spectra were collected and subtracted at each temperature and measurements were taken in a wavenumber range of 500-4000 cm^{-1} .

Baseline subtractions of FTIR data were done using the Rubberband method (64 ranges, 8 iterations) in the Data Exploration, Visualization, and Analysis for Spectroscopy (DEVAS) software (<http://nemo.mtholyoke.edu>) [Carey et al., 2017]. The data was then normalized to a user-defined value of 3600 cm^{-1} .

3.4 Raman Spectroscopy

Raman measurements were collected at the Bruker Optics Inc. office in Billerica, MA using a Bruker SENTERA II Confocal Raman Microscope. First, a small piece of römerite (CIT-15681-C,D,E) was loaded into an Instec HCP621G gas tight plate with a silver heating and cooling block. The plate was then loaded into the Raman spectrometer. Measurements were taken with a 523 nm, 25 mW laser. The spectrometer has a spectral resolution of 4 cm^{-1} and spectra was collected within a 50-4250 cm^{-1} range. The integration time of each measurement was 20 seconds

and two coadditions were performed to eliminate noise from cosmic rays.

The first Raman measurement was taken at 23.4°C. The temperature was then cooled to -120°C or around 153K. Next, the temperature was increased back to 20°C in increments of 10°C.

Baseline subtractions were performed using the Rubberband method (68 ranges, 4 iterations) in DEVAS. Spectra were also normalized to a user-defined value of 1116 cm^{-1} in DEVAS.

3.5 Mössbauer Spectroscopy

Mössbauer spectroscopy measurements were performed using a W203 Mössbauer spectrometer at Mount Holyoke College. First, 30 mg of römerite powder (CIT-15681-C,D,E) were ground with white sugar and mounted within a plastic washer, sealed at both ends using Kapton tape. Measurements were taken at 295, 275, 250, 225, 200, 175, 150, 125, 100, 80, 60, 40, 12, 8, and 4K using a Janus closed-cycle He compressor for temperatures less than 295K. At each temperature, the spectrum was folded about the midpoint. The spectra were calibrated to an α -Fe foil using the WMOSS4 program.

Spectra were fit using Mexdisdd program which solves the full hyperfine interaction Hamiltonian to minimize the χ^2 deviation between the data and the model [Vandenberghe et al., 1994].

Chapter 4

RESULTS

4.1 X-ray Diffraction

At ambient environmental conditions, the refined unit cell parameters of römerite are: $a = 6.452(2) \text{ \AA}$, $b = 15.316(4) \text{ \AA}$, $c = 6.319(3) \text{ \AA}$, $\alpha = 90.16(2)^\circ$, $\beta = 100.95(2)^\circ$, $\gamma = 85.84(2)^\circ$, $V = 611.3(7) \text{ \AA}^3$. Consistent with previous studies of römerite's crystal structure, the sample crystallizes in the triclinic $P\bar{1}$ space group. Its structure consists of Fe^{2+} octahedra coordinated with six H_2O molecules [$\text{Fe}^{2+}(\text{H}_2\text{O})_6$] as well as Fe^{3+} octahedra coordinated with four H_2O molecules and two O^{2-} atoms. These oxygen anions are shared with two sulfate tetrahedra to form $\text{Fe}^{3+}(\text{SO}_4)_2(\text{H}_2\text{O})_4$ clusters. Römerite's crystal structure is illustrated in Figure 4.1.

X-ray diffraction measurements indicate that the lattice lengths a and b decrease, while c increases with decreasing temperature. Likewise, with decreasing temperature, the lattice angles α and β decrease, while γ increases. Graphs of each lattice parameters' and angles' evolution with temperature are provided in Figure 4.2.

The unit cell volume of römerite decreases with decreasing temperature. These data are shown in Figure 4.3 and compared with the unit cell data of several other minerals in Figure 4.4. The latter graph confirms that very hydrated minerals are increasingly compressible with temperature. Römerite as well as blödite, kieserite, and szomolnokite are all hydrous sulfates (Table 2.1). These are compared to the silicate bridgmanite, and the hydroxide boehmite, which experience far less

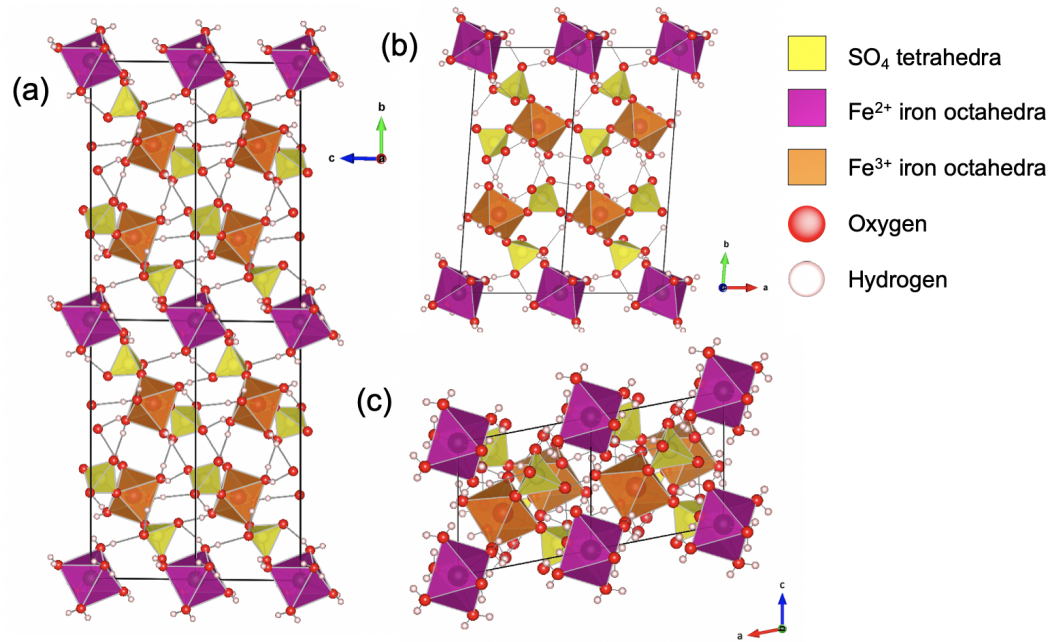


Figure 4.1: Crystal structure of römerite at three different orientations.

compression in unit cell volume with temperature when compared to the hydrous sulfates.

Thermal expansion values of römerite's unit cell dimensions were calculated from 100-300K and included data from the forward and reverse temperature series. First, Matlab's curve-fitting tool was used to make polynomial fits of each lattice parameters' change with temperature. With these fits, the thermal expansion values for each lattice parameter were solved using the following equation,

$$\alpha = \frac{1}{L} \frac{\partial L}{\partial T},$$

where α is the thermal expansion coefficient and L is a unit cell dimension. The calculated thermal expansion values at room temperature are $\alpha_a = 6.7(5) \times 10^{-5}$

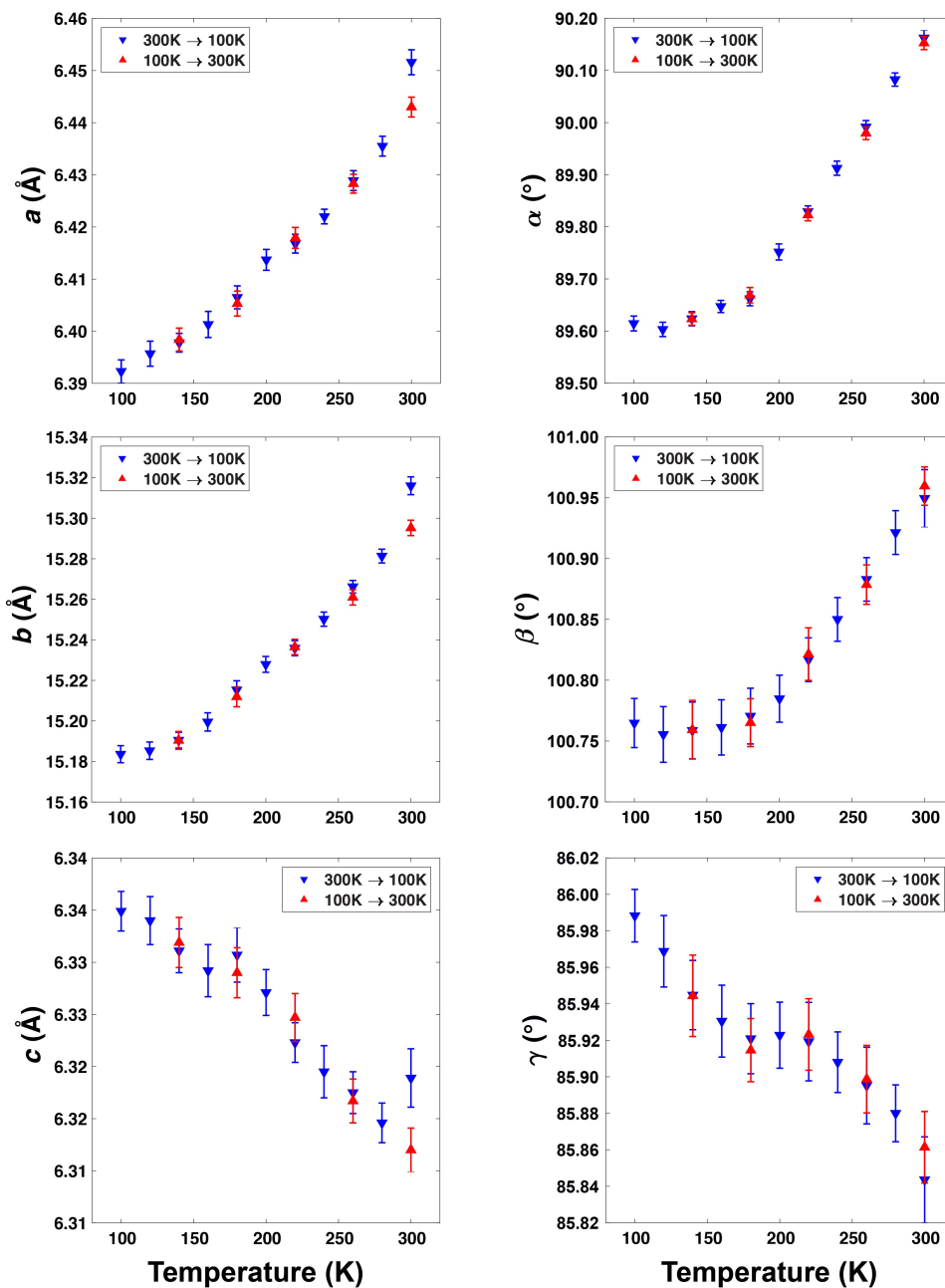


Figure 4.2: Temperature dependence of römerite's lattice parameters a , b , c and lattice angles α , β , and γ .

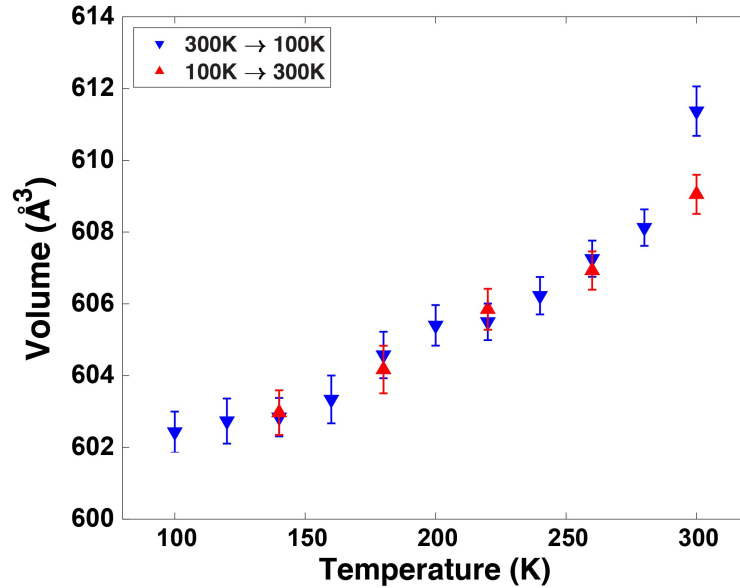


Figure 4.3: Temperature dependence of römerite's unit cell volume

K^{-1} , $\alpha_b = 6.6(3) \times 10^{-5} \text{ K}^{-1}$, $\alpha_c = -2.1(5) \times 10^{-5} \text{ K}^{-1}$, and $\alpha_{vol} = 1.0(1) \times 10^{-5} \text{ K}^{-1}$. The magnitude of the c lattice parameter's thermal expansion is smaller than for a and b , and more notably, its thermal expansion value experiences a sign change.

To calculate the error of the thermal expansion coefficients, a normal distribution within the error of each lattice parameter data point was created. This distribution was truncated at ± 0.25 of its FWHM. For each point, a random value was selected within this truncated distribution, and a polynomial fit was performed with these random points. This process was repeated 100 times and each set of polynomial fit parameters were saved. The average of each parameter resulting from 100 iterations is reported. The standard deviation was propagated to calculate the thermal expansion coefficient and error at each temperature.

Bond length and angle data from the XRD measurements are still under review.

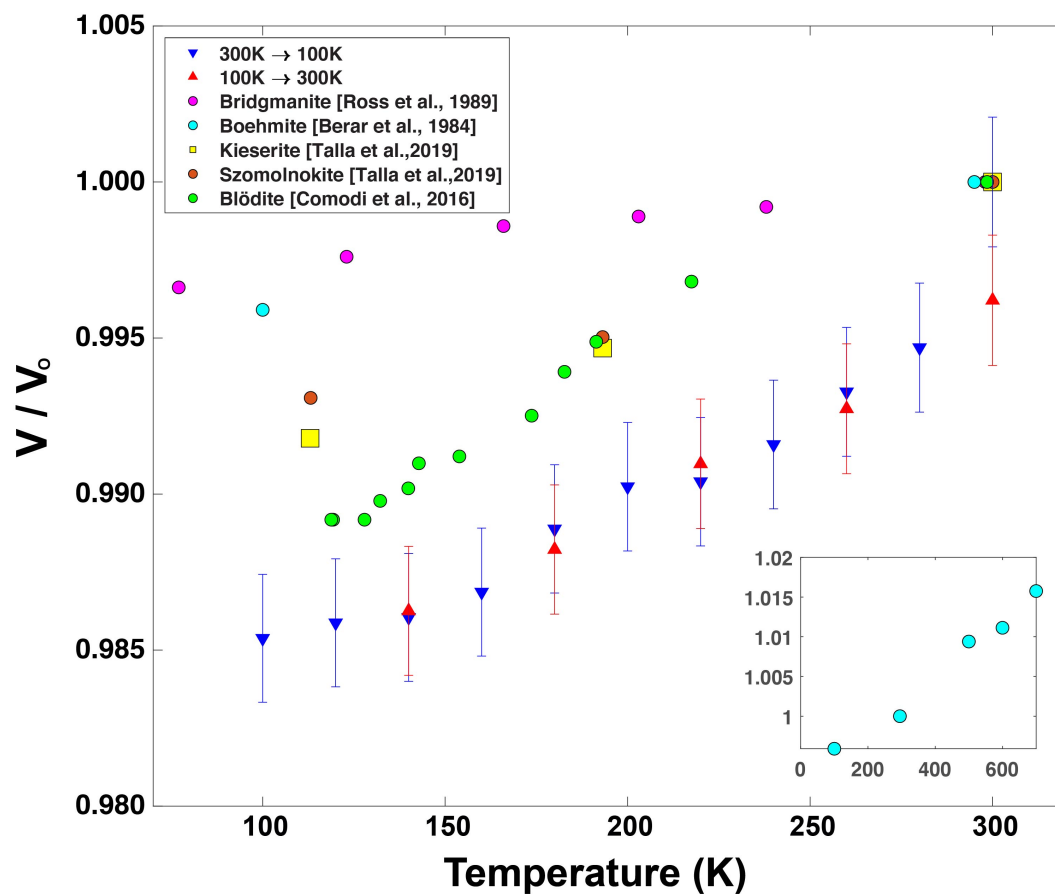


Figure 4.4: Comparison of the volume temperature dependence of römerite, other hydrous sulfates [Talla and Wildner, 2019; Comodi et al., 2017], the silicate bridgmanite [Ross and Hazen, 1989], and the hydroxide boehmite [Berar et al., 1984].

However, select bond lengths and angles were plotted with temperature for a preliminary assessment. In particular, Fe^{3+} and O^{-2} bonds are observed along with sulfur and oxygen bonds and S-O-Fe^{3+} angles. The temperature evolution of these parameters is shown in Figure 4.5.

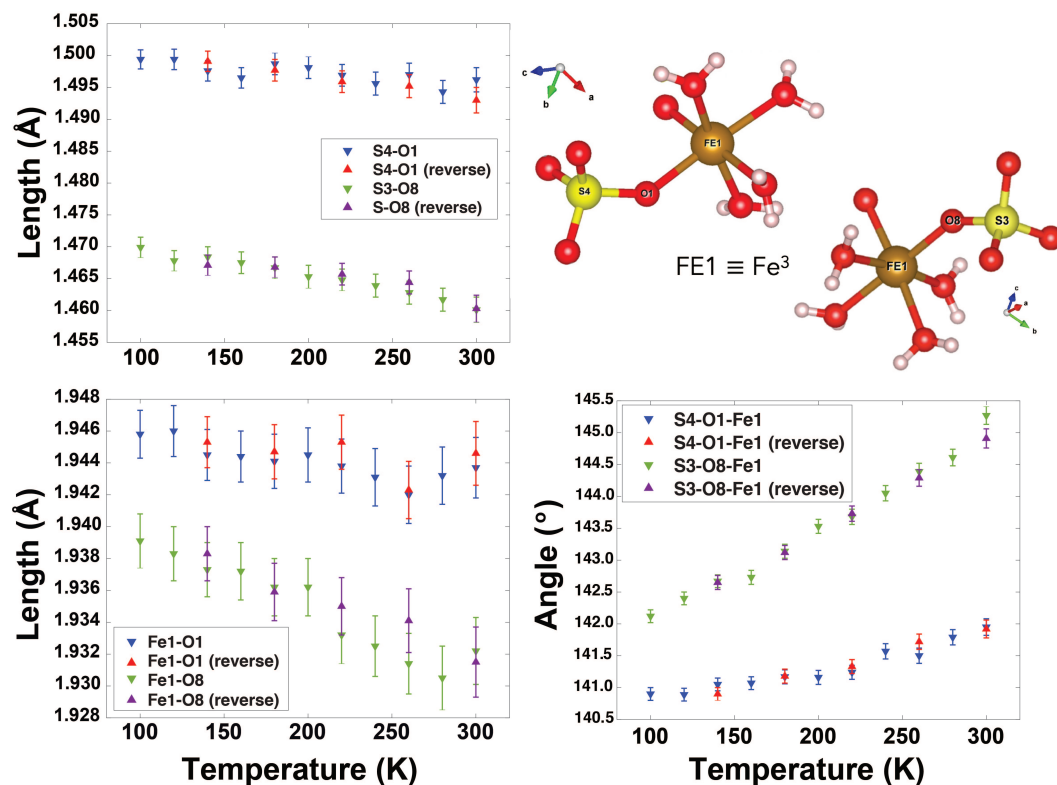


Figure 4.5: Temperature dependence of a select few S–O and Fe–O bond lengths and S–O–Fe bond angles.

4.2 Fourier-Transform Infrared Spectroscopy

SO₄ has four fundamental modes: symmetric stretching (ν_1) and bending (ν_2) and asymmetric stretching (ν_3) and bending (ν_4) at 983, 450, 1105, and 611 cm⁻¹, respectively [Nakamoto, 2009]. Two of these modes, asymmetric stretching and asymmetric bending, are IR-active, while all of them are Raman-active [Ling and Wang, 2010].

Liquid H₂O has three fundamental modes, all of which are IR and Raman-active [Vandenabeele, 2013]. H–O–H symmetric (ν_1) and asymmetric stretching (ν_3) occur at 3450 cm⁻¹ and 3615 cm⁻¹, respectively, and the H–O–H bending mode

(ν_2) occurs at 1640 cm^{-1} [Nakamoto, 2009].

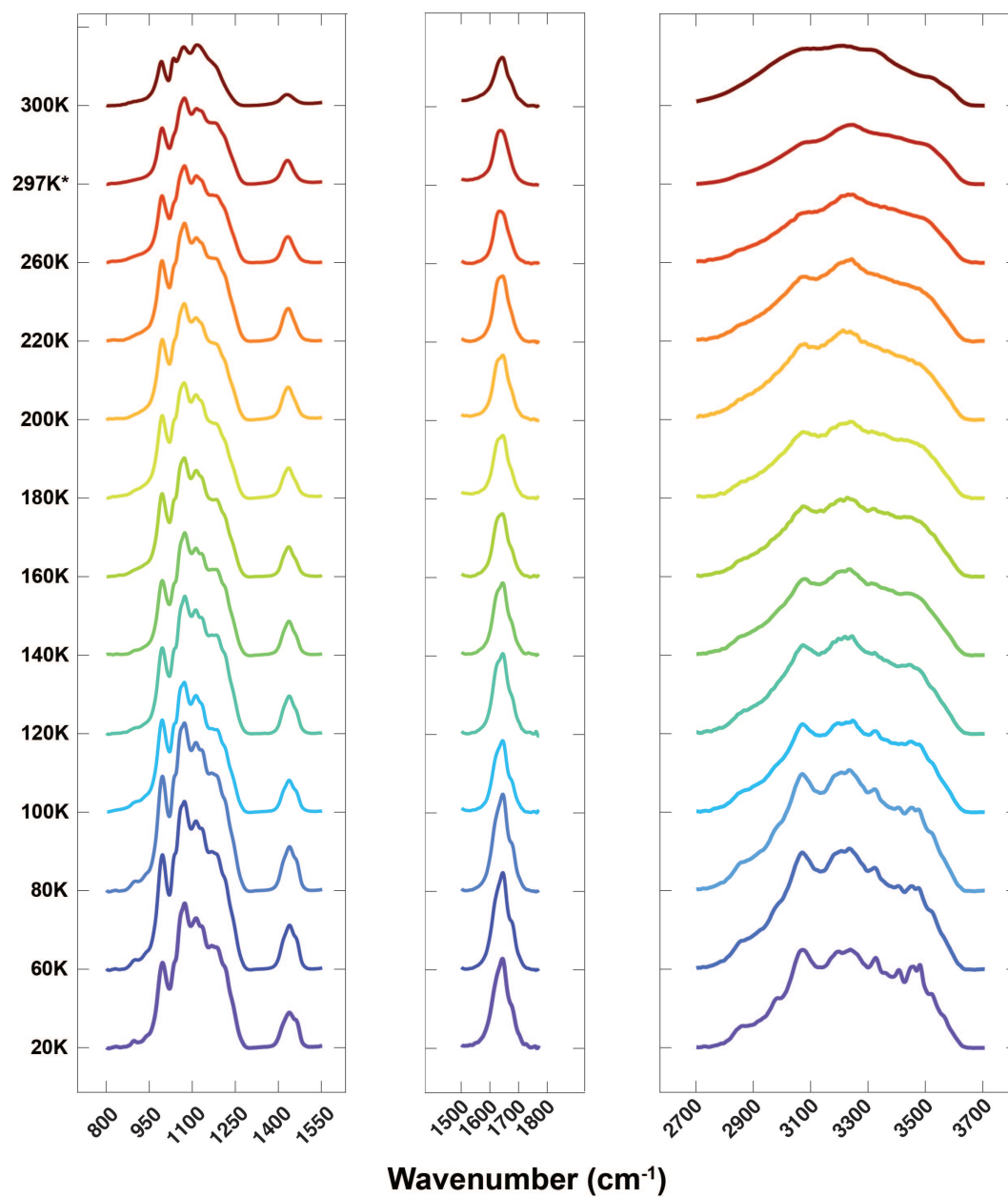


Figure 4.6: Infrared spectra from 20-300K, separated into three relevant regions. Each region has its own intensity scale. Thus, inter-regional intensity comparisons should not be made. The 297K spectrum was taken before the sample was cooled to 20K and reheated to 300K.

Table 4.1: Approximate band assignments of römerite's infrared spectrum at 20K.

Wavenumber (cm ⁻¹)	Band Assignment	Source
897	Libration	Frost (2011)
996	TBD	
1073	$\nu_3(\text{SO}_4)$	Sobron (2011), Mauro (2019)
1113	$\nu_3(\text{SO}_4)$	Sobron (2011), Mauro (2019)
1131	$\nu_3(\text{SO}_4)$	Sobron (2011), Mauro (2019)
1168	$\nu_3(\text{SO}_4)$	Sobron (2011), Mauro (2019)
1183	$\nu_3(\text{SO}_4)$	Sobron (2011), Mauro (2019)
1213	$2\nu_4(\text{SO}_4)$	
1439	Impurity	Majzlan (2011)
1644	$\nu_1(\text{H}_2\text{O})$	Nakamoto (2009)
2859	Impurity	Majzlan (2011)
2985	$3\nu_1(\text{SO}_4)$ or Impurity	Majzlan (2011)
3073	$\nu_1(\text{H}_2\text{O})$	
3198	$\nu_1(\text{H}_2\text{O})$	Sobron (2011)
3240	$\nu_1(\text{H}_2\text{O})$	Mauro (2019)
3326	$\nu_1(\text{H}_2\text{O})$ or $3\nu_3(\text{SO}_4)$	Mauro (2019)
3362	$\nu_1(\text{H}_2\text{O})$	Mauro (2019)
3409	$\nu_1(\text{H}_2\text{O})$	Mauro (2019)
3455	$\nu_1(\text{H}_2\text{O})$	Mauro (2019)
3481	$\nu_1(\text{H}_2\text{O})$	Mauro (2019)
3521	$\nu_1(\text{H}_2\text{O})$ or $\nu_3(\text{H}_2\text{O})$	Mauro (2019)
3568	$\nu_1(\text{H}_2\text{O})$ or $\nu_3(\text{H}_2\text{O})$	Mauro (2019)

Thus, the FTIR spectrum of römerite is best analyzed in three different wavenumber regions. Bands in the region from 800-1550 cm⁻¹ are assigned to the asymmetric stretching (ν_3) mode and the first overtone of the asymmetric bending mode (ν_4) of the sulfate anion. Bands in the second region from 1500-1800 cm⁻¹ are assigned to the H–O–H bending mode. Finally, the remaining H–O–H modes are found in the final region from 2700-3700 cm⁻¹, including the symmetric and antisymmetric stretching modes. Normalized and offset FTIR spectra at each temperature are

presented in Figure 4.6. The 40K spectrum was removed from the data set due to instrument error. Approximate band assignments are listed in Table 4.1. Assignments preceded by the number 2 or 3 are first or second overtones, respectively. Furthermore, assignments labelled as librations arise due to hindered rotations of the water molecules. These rotations are either rocking, wagging, or twisting motions [Lepodise et al., 2013].

A single peak at around 1439 cm^{-1} and a low intensity peak at 2859 cm^{-1} are likely the vibrational modes of a carbon-based contaminant in the sample and will not be considered in the analysis. Majzlan et al. (2013) also observes peaks in these regions, attributing them to carbon impurities.

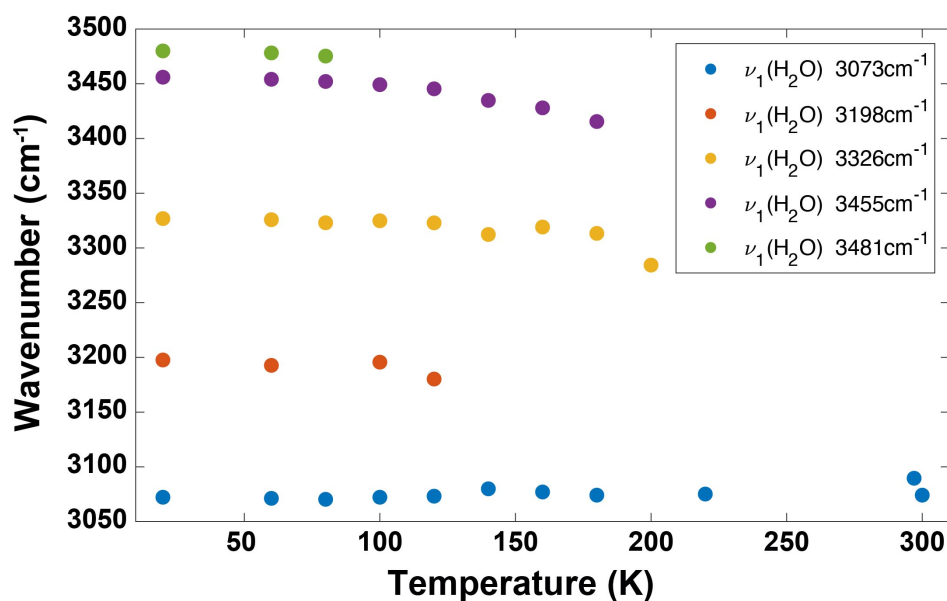


Figure 4.7: Temperature dependence of a select few bands corresponding to the first fundamental vibration of H_2O . Refer to Table 4.1 for more information about band assignments.

Under these normalization conditions, a striking decrease in band intensity occurs

with increasing temperature. This is observed in each region of interest. Furthermore, preliminary tracking of several $\nu_1\text{H}_2\text{O}$ peaks with temperature shows small changes in their positions (Figure 4.7). In general, most of the observed peaks decrease only slightly with increasing temperature.

4.3 Raman Spectroscopy

The Raman spectrum of römerite, which spans a greater range of wavenumbers than the FTIR spectrum, is best split into four regions. The first region from 50-750 cm^{-1} includes fundamental vibrations of Fe–O bonds [Sobron and Wang, 2012; Mauro et al., 2019]. However, this region is still under evaluation. Bands in the region from 900-1350 cm^{-1} are assigned to the four fundamental modes of the sulfate anion. The two most intense peaks found at around 1011 cm^{-1} and 1038 cm^{-1} are assigned to the $\nu_1(\text{SO}_4)$ mode. Observing multiple bands for one mode assignment suggests that the functional group in question occurs at non-equivalent sites in the sample [Frost et al., 2011; Sobron and Wang, 2012; Mauro et al., 2019]. Thus, the presence of these two distinct bands at all temperatures is likely indicative of two different sulfate sites in the structure of römerite, generally designated as Fe1 and Fe2 [Sobron and Wang, 2012]. These two peaks were also observed by Frost et al. (2011) in their Raman spectroscopic study of römerite. The large peak and small shoulder in the region from 1500-1800 cm^{-1} are assigned to the bending mode of H_2O . Finally, the last region from 2650-3850 cm^{-1} includes the antisymmetric and symmetric stretching modes of water. Approximate Raman band assignments are listed in Table 4.2.

Similarly to the FTIR spectra, a significant and smooth decrease in band intensity is

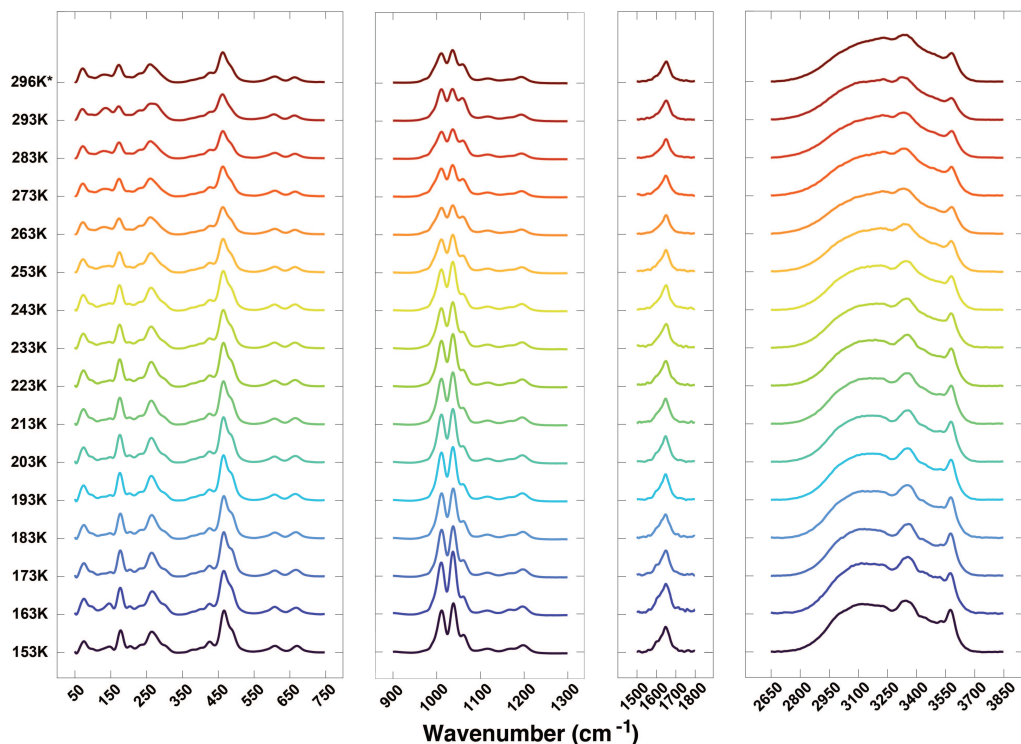


Figure 4.8: Raman spectra from 150-300K, separated into four relevant regions. Each region has its own intensity scale. Thus, inter-regional intensity comparisons should not be made. The 296K* spectrum was taken before the sample was cooled to 153K and reheated to 293K.

observed with increasing temperature in the Raman spectra. This pattern is striking among the two $\nu_1(\text{SO}_4)$ peaks, while the small shoulder at 1061 cm^{-1} maintains the same intensity at all temperatures. Future exploration of these data should include how the relative intensities of these three peaks change with temperature. This pattern is also seen in the water and low-wavenumber regions of the spectra.

4.4 Mössbauer Spectroscopy

Low-temperature results from Mössbauer experiments on the römerite sample are still under review. Room temperature data, however, are included in this section.

Table 4.2: Approximate band assignments of römerite's Raman spectrum at 20K.

Wavenumber (cm ⁻¹)	Band Assignment	Source
75	TBD	
100	TBD	
146	TBD	
178	TBD	
204	TBD	
233	TBD	
264	TBD	
302	TBD	
377	TBD	
399	$\nu_2(\text{SO}_4)$	Mauro (2019)
426	$\nu_2(\text{SO}_4)$	Mauro (2019), Sobron (2011)
466	$\nu_2(\text{SO}_4)$	Mauro (2019), Sobron (2011)
608	$\nu_4(\text{SO}_4)$	Mauro (2019), Sobron (2011)
669	$\nu_4(\text{SO}_4)$	Mauro (2019), Sobron (2011)
903	Libration	Frost (2010)
1011	$\nu_1(\text{SO}_4)$	Mauro (2019)
1038	$\nu_1(\text{SO}_4)$	Mauro (2019)
1061	$\nu_3(\text{SO}_4)$	Mauro (2019)
1117	$\nu_3(\text{SO}_4)$	Mauro (2019), Sobron (2011)
1168	$\nu_3(\text{SO}_4)$	Mauro (2019), Sobron (2011)
1197	$\nu_3(\text{SO}_4)$	Mauro (2019)
1647	$\nu_2(\text{H}_2\text{O})$	Nakamoto, Mauro (2019)
1599	$\nu_2(\text{H}_2\text{O})$	Nakamoto, Mauro (2019)
3115	$\nu_1(\text{H}_2\text{O})$	Mauro (2019)
3226	$\nu_1(\text{H}_2\text{O})$	Mauro (2019)
3345	$\nu_1(\text{H}_2\text{O})$	Mauro (2019)
3446	$\nu_1(\text{H}_2\text{O})$	Mauro (2019)
3523	$\nu_1(\text{H}_2\text{O})$ or $\nu_3(\text{H}_2\text{O})$	Mauro (2019)
3527	$\nu_1(\text{H}_2\text{O})$ or $\nu_3(\text{H}_2\text{O})$	Mauro (2019)

Fe^{3+} exists in römerite's structure in octahedral sites, forming $\text{Fe}^{3+}(\text{SO}_4)_2(\text{H}_2\text{O})_4$ clusters. Fe^{2+} also occurs in an octahedral site in römerite, forming a $\text{Fe}^{2+}(\text{H}_2\text{O})_6$

Table 4.3: Mössbauer parameters of römerite. The parameters δ and Δ are expressed in mm/s units.

Temperature (K)	δ							
295	0.463	0.19	0.343	0.459	1.269	3.207	1.259	3.381

cluster. The Mössbauer transmission spectrum for römerite at 295K is shown in Figure 4.9. At room temperature, there are four Fe sites: an Fe^{3+} singlet, an Fe^{3+} doublet, and two Fe^{2+} doublets. These site assignments were made according to several assumptions: IS for $\text{Fe}^{2+} \gg$ IS for Fe^{3+} , and QS for $\text{Fe}^{2+} \gg$ QS for Fe^{3+} .

Room temperature Mössbauer parameters of römerite, shown in Table 4.3, are consistent with several other Mössbauer studies of römerite. Dyar et al. (2013) found $\delta = 0.43 - 0.47$ mm/s and $\Delta = 0.23 - 0.55$ mm/s for Fe^{3+} sites, and $\delta = 1.23 - 1.39$ mm/s and $\Delta = 2.09 - 3.92$ for Fe^{2+} sites. Majzlan et al. (2011) reports low-temperature (80K) parameters for two Fe^{3+} sites: $\delta = 0.52$ mm/s and $\delta = 0.59$ mm/s and $\Delta = 0.38$ mm/s and $\Delta = 0.17$ mm/s, respectively. They also report a Fe^{2+} doublet with $\delta = 1.38$ mm/s and $\Delta = 3.49$ mm/s. Rothstein et al. (2005) reports parameters from 210-270K. At 270K, they report one Fe^{2+} site, $\delta = 1.297$ mm/s and $\Delta = 2.918$ mm/s, and one Fe^{3+} site, $\delta = 0.340$ mm/s and $\Delta = 0.606$ mm/s.

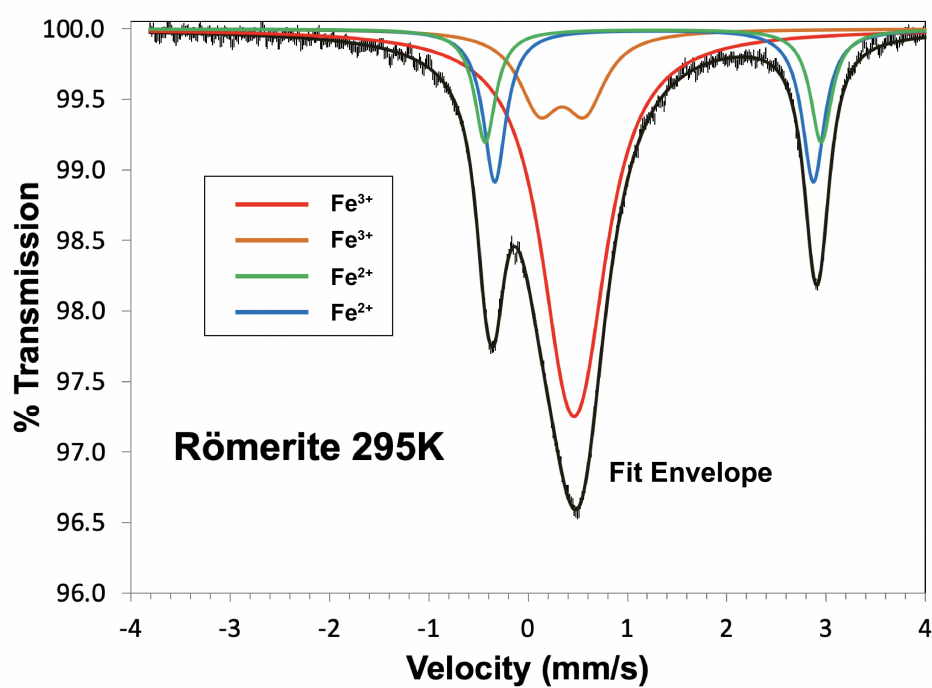


Figure 4.9: Mössbauer transmission spectrum of römerite at 295K.

Chapter 5

DISCUSSION

It is expected that absorption band widths will decrease with decreasing temperature. This is observed in both the Raman and FTIR data in this study, where peaks at lower temperatures are better resolved than in higher temperature spectra. As the sample is heated, these sharp peaks begin to widen and overlap due to thermal broadening of the sample [Sobron and Wang, 2012]. Recall that according to the more accurate anharmonic model of a molecule's potential energy, excitations and relaxations between higher-energy vibrational states are less energetic than transitions between lower energy states. At warmer temperatures, the molecules in a crystal have more freedom to assume higher energy vibrational states [Atkins and Paula, 2006]. Therefore, a broader range of energies is absorbed as more transitions between these high energy states occur [Koike et al., 2006]. At low temperatures, molecules are restricted to their lower energy vibrational states [Atkins and Paula, 2006]. Therefore, there is less variability in absorbed transition energies. This produces the sharpening effect seen in low-temperature spectra.

Because of thermal broadening with increasing temperature, it can be difficult to characterize bands at room temperature. Rather, the the fine structures present in low-temperature spectra can be used to assign bands. These assignments are given in Tables 4.1 and 4.2.

Preliminary analysis of band positions shows that some peaks attributed to stretching modes in H₂O increase in wavenumber with decreasing temperature (Figure 4.7).

This is consistent with observed contraction of the römerite unit cell. As the sample is cooled, H–O bonds in its structure likely contract, increasing their force constants, or strengths. Recall that Equations 2.6 and 2.7 suggest an increase in force constant will increase the energies associated with a molecule's vibrations. Energy is proportional to wavenumber. Thus, in decreasing temperature, the vibrational energies of water increase and the wavenumbers of their bands increase [Bowey et al., 2001].

Some bonds in the römerite structure may be less compressible than others [Bowey et al., 2001]. In fact, Figure 4.5 shows several bonds that actually increase in length with decreasing temperature. Further X-ray diffraction analysis of how bond lengths change with temperature will reveal which are the most compressible. These can then be compared to shifts in band positions corresponding to bond lengths of interest.

It is also possible that as the temperature is lowered, some entirely new bands will appear. In their analysis of hydrous sulfates at low temperatures (178-294K), Sobron et al. (2012) attributes this to an increase in the structural ordering of water at low temperatures. However, to differentiate between what peaks manifest only at low temperatures and which are present through the entire temperature series, a thorough peak-fitting process must occur, and this is a next step to pursue.

In conducting the X-ray diffraction, FTIR spectroscopy, and Raman spectroscopy experiments, an initial measurement was taken at room temperature. Next, the temperature was cooled to its minimum and heated back to room temperature. At that point, another measurement was taken. As a result, there are two measurements at

room temperature, referred to here as the forward and the reverse room temperature (RT) measurements, respectively. In each of these methods, a discrepancy is observed between the forward and reverse RT measurement.

For the X-ray diffraction data, this discrepancy is seen prominently in all lattice axes lengths (Figure 4.2), the γ angle (Figure 4.2), the volume (Figure 4.3), and several bond lengths/angles (Figure 4.5). Hysteresis was considered, but deemed unlikely as all other data points remain consistent within error between the forward and reverse temperature series.

Furthermore, this behavior at room temperature is evident in the synchrotron infrared spectroscopy temperature series, particularly in the differences between the 297K forward-RT spectrum and the 300K reverse-RT spectrum (Figure 4.6). Although less prominent, the discrepancy is also observed between the 296K forward-RT spectrum and the 293K reverse-RT spectrum in the Raman data (Figure 4.8).

There are several plausible reasons for this inconsistency. First, it is possible that in cooling the sample, water molecules in the römerite structure undergo an irreversible shift in orientation. When returning to room temperature, the water molecules can no longer fit in the same site as they did during the forward-RT measurement. Thus, the sample undergoes an isochemical change; it is still römerite, but some atomic positions have shifted appreciably, changing its local molecular environment. This hypothesis is consistent with the aforementioned structural ordering proposed by Sobron et al. (2012). It is as-yet unclear how stable this transition is.

Second, it is possible that römerite undergoes a phase change at some point in the temperature series. Thus, when the reverse-RT measurement is taken, the

sample is no longer r merite. Dehydration is a common problem when studying very hydrated minerals at different temperatures. Therefore, it is possible that the sample dehydrated when heated to room temperature, potentially explaining the discontinuity. However, phase changes will often manifest as more dramatic transformations in the lattice parameters and the infrared spectra of a sample. X-ray diffraction data was also revisited to ensure that at each temperature, the sample still fell within the same accepted parameters of r merite.

Therefore, current evidence suggests that the most likely cause of this discrepancy at room temperature is a significant structural change among the water molecules that results from lowering the ambient temperature past a certain threshold. Clearly, the discrepancy between the forward-RT (296K) and reverse-RT (293K) Raman measurements is far less profound than it is for the infrared measurements. This can be attributed to the difference in temperature intervals between the two experiments. While the temperature of the FTIR sample was lowered to 20K, the temperature of the Raman sample did not cool below 153K. Thus, it is likely that the water molecules in the Raman sample did not undergo such dramatic and permanent changes.

The significant change in intensity seen in both sets of molecular spectroscopy data must also be addressed. Changes in intensity correlated with changes in peak sharpness and peak position with temperature have been observed in several studies of minerals under variable temperature conditions [Day, 1976; Koike et al., 2006; Volkov et al., 2021]. However, the exact reasons behind changes in intensity in spectra from this study are still under consideration and will depend on the final method of normalization.

Future analysis of low-temperature Mössbauer data will certainly deepen understanding of the mechanisms most responsible for the distortion of römerite. Observing how isomer shift and quadrupole splitting parameters evolve with temperature may reveal how the coordination environment and site geometry of iron changes as römerite contracts. Further analysis of the low wavenumber regions of the Raman data, which can be attributed to Fe–O vibrations, may prove complementary.

Chapter 6

CONCLUSION

There are several potential avenues to improve the analysis of the temperature dependence of römerite. First, the methodology for normalizing the infrared and Raman data should be reassessed. This procedure is convoluted by the complexity of the römerite spectrum, and will likely require further experimentation. Upon the satisfactory completion of this step, a thorough peak-fitting procedure of the Raman and FTIR data will be done to precisely differentiate between bands that appear only at certain temperatures and bands that simply broaden and overlap with others. Further, this approach will allow the temperature evolution of all bands to be observed. Next, additional research is necessary to explore the lower wavenumber region of the Raman data, which likely includes information about the fundamental vibrations of Fe–O. Likewise, analyzing low-temperature Mössbauer data will further the investigation of iron in the sample.

Additional research on römerite, including an additional series of X-ray diffraction, FTIR, and Raman measurements is planned. X-ray diffraction measurements will be done with an extended temperature series ranging from 100 to 320K. Exploring temperatures slightly higher than room temperature may provide more insight into the potential isochemical change observed in the initial round of data. Moreover, by using a larger single crystal sample, the temperature intervals can be shortened, providing a more nuanced image of römerite's structural deformation. The original X-ray diffraction measurements were acquired as the sample was cooled and heated

back to room temperature. This provided valuable insight into the reversibility of römerite's structural deformation and should be repeated in future infrared and Raman experiments for consistency.

While these corroborating analyses are ongoing, several firm conclusions can be made. Most significantly, the practice of using room temperature data to interpret spectroscopy data of planetary surfaces is prone to error. Microscopic changes in the structure of hydrated minerals due to temperature will manifest as large changes in the band position, width, and intensity on an infrared spectrum. Often, the most intense changes occur in regions containing the fundamental vibrations of water. As such, this observation is relevant to not simply römerite and hydrous sulfates, but to all hydrated mineral phases. In conducting further spectral research of planetary surfaces, every effort should be made to compare planetary data to laboratory spectra in a relevant temperature range. This endeavor can be further expanded and has been highlighted by Sobron et al., (2012) in their work studying minerals at relevant temperature and pressure conditions. It is also expected that Mössbauer spectra will change with temperature, and because Mössbauer spectroscopy is a common method for identifying samples on Mars, the degree of its temperature dependence should be further explored.

Pressure is known to structurally deform a crystal lattice, and therefore affect band appearance on an infrared spectrum [Postmus et al., 1968]. Consequently, the most accurate comparisons can be made when both pressure and temperature are taken into consideration. This combination is also relevant in considering how minerals cycle through the interiors of planetary bodies, carrying water with them. Thus, future studies of römerite will include pressure-dependant data, further expanding

the quality of our analysis as it applies to planetary surface and interior properties.

BIBLIOGRAPHY

- Ameh, Enefolo S. (2019). “A review of basic crystallography and x-ray diffraction applications”. In: *The International Journal of Advanced Manufacturing Technology*.
- Atkins, Peter and Julio de Paula (2006). *Atkins' Physical Chemistry*. W.H. Freeman and Company, pp. 560–589. ISBN: 0716787598.
- Balkanski, M., R. F. Wallis, and E. Haro (Aug. 1983). “Anharmonic effects in light scattering due to optical phonons in silicon”. In: *Phys. Rev. B* 28 (4), pp. 1928–1934. DOI: 10.1103/PhysRevB.28.1928.
- Berar, J.F., D. Grebille, P. Gregoire, and D. Weigel (1984). “Thermal expansion of boehmite. An anomaly near 560 K due to non-stoichiometric water”. In: *Journal of Physics and Chemistry of Solids* 45.
- Bibring, Jean-Pierre, Yves Langevin, A. Gendrin, Brigitte Gondet, François Poulet, Michel Berthé, Alain Soufflot, Ray Arvidson, Nicolas Mangold, John Mustard, and Pierre Drossart (Apr. 2005). “Mars Surface Diversity as Revealed by the OMEGA/Mars Express Observations”. In: *Science (New York, N.Y.)* 307, pp. 1576–81. DOI: 10.1126/science.1108806.
- Bowey, J.E., C. Lee, C. Tucker, A.M. Hofmeister, P.A.R. Ade, and M.J. Barlow (Aug. 2001). “Temperature effects on the 15–85 μm spectra of olivines and pyroxenes”. In: *Monthly Notices of the Royal Astronomical Society* 325.2, pp. 886–896. DOI: 10.1046/j.1365-8711.2001.04523.x.
- Carey, C., M. D. Dyar, T. Boucher, and S. Giguere (2017). “Web-based software for preprocessing, matching, fitting, prediction, and visualization of spectroscopic data: the data exploration, visualization, and analysis of spectra”. In.
- Carlson, R., W. Calvin, James Dalton, G. Hansen, Reggie Hudson, R. Johnson, Thomas Mccord, and M. Moore (Jan. 2009). “Europa's Surface Composition”. In: *Europa*, pp. 283–.
- Choudhary, Shalini, Prabhat Ranjan, and Tanmoy Chakraborty (2020). “Atomic polarizability: A periodic descriptor”. In: *Journal of Chemical Research* 44.3-4, pp. 227–234. DOI: 10.1177/1747519819889936.
- Comodi, Paola, Vincenzo Stagno, Azzurra Zucchini, Yingwei Fei, and Vitali Prakapenka (2017). “The compression behavior of blödite at low and high temperature up to 10GPa: Implications for the stability of hydrous sulfates on icy planetary bodies”.

- In: *Icarus* 285, pp. 137–144. ISSN: 0019-1035. DOI: <https://doi.org/10.1016/j.icarus.2016.11.032>.
- Dalton, J., James Shirley, and L. Kamp (Mar. 2012). “Europa’s icy bright plains and dark line: Exogenic and endogenic contributions to composition and surface properties”. In: *Journal of Geophysical Research (Planets)* 117, pp. 3003–. DOI: 10.1029/2011JE003909.
- Dalton, J. B. (2007). “Linear mixture modeling of Europa’s non-ice material based on cryogenic laboratory spectroscopy”. In: *Geophysical Research Letters* 34.
- Day, Kenrick L. (Jan. 1976). “Temperature Dependence of Mid-Infrared Silicate Absorption”. In: 203, p. L99. DOI: 10.1086/182028.
- Ding, J. J., Philippe Boduch, Alicja Domaracka, Stéphane Guillous, Thomas Langlinay, X. Y. Lv, M. E. Palumbo, Hermann Rothard, and Giovanni Strazzulla (2013). “Implantation of multiply charged sulfur ions in water ice”. In: *Icarus* 226, pp. 860–864.
- Dyar, D. M., David G. Agresti, Martha W. Schaefer, Christopher A. Grant, and Elizabeth C. Sklute (2006). “Mössbauer Spectroscopy on Earth and Planetary Materials”. In: *Annual Review of Earth and Planetary Sciences* 34.1, pp. 83–125. DOI: 10.1146/annurev.earth.34.031405.125049.
- Dyar, M. D., Elly Breves, Erica Jawin, Gerard Marchand, Melissa Nelms, V. A. O’Connor, Samantha E. Peel, Yarrow Rothstein, Elizabeth C. Sklute, Melissa D. Lane, Janice L. Bishop, and Stanley A. Mertzman (2013). “What Lurks in the Martian Rocks and Soil? Investigations of Sulfates, Phosphates, and Perchlorates. Mössbauer parameters of iron in sulfate minerals”. In: *American Mineralogist* 98, pp. 1943–1965.
- Dyar, M. D. and Elizabeth C. Sklute (2019). “Mössbauer Spectroscopy: Theory and Laboratory Spectra of Geologic Materials”. In: *Remote Compositional Analysis: Techniques for Understanding Spectroscopy, Mineralogy, and Geochemistry of Planetary Surfaces*. Ed. by Janice L. Bishop, James F. Bell III, and Jeffrey E. Editors Moersch. Cambridge Planetary Science. Cambridge University Press, pp. 147–167. DOI: 10.1017/9781316888872.009.
- Dyar, D. M. and Mickey Gunter (Aug. 2008). “Mineralogy and Optical Mineralogy”. In: *American Mineralogist* 93.8-9, pp. 1481–1482. ISSN: 0003-004X. DOI: 10.2138/am.2008.524.
- Fanfani, L, A. Nunzi, and P. F. Zanazzi (1970). “The crystal structure of roemerite”. In: *American Mineralogist* 55, pp. 78–89.

- Frost, Ray L., Sara J. Palmer, Jiri Cejka, Jiri Sejkora, Jakub Plasil, Ivana Jebava, and Eloise C. Keeffe (2011). “A Raman spectroscopic study of M2+M3+ sulfate minerals, römerite $\text{Fe}^{2+}\text{Fe}^{3+}_2(\text{SO}_4)_4 \cdot 14\text{H}_2\text{O}$ and botryogen $\text{Mg}^{2+}\text{Fe}^{3+}(\text{SO}_4)_2(\text{OH}) \cdot 7\text{H}_2\text{O}$ ”. In: *Journal of Raman Spectroscopy* 42, pp. 825–830.
- Gendrin, Aline, Nicolas Mangold, J. P. Bibring, Y. Langevin, B. Gondet, François Poulet, G. Bonello, Cathy Quantin, John F. Mustard, Raymond E. Arvidson, and S. Lemouélic (2005). “Sulfates in Martian Layered Terrains: The OMEGA/Mars Express View”. In: *Science* 307, pp. 1587–1591.
- Hawthorne, Frank, Sergey Krivovichev, and Peter Burns (Jan. 2000). “The Crystal Chemistry of Sulfate Minerals”. In: *Sulfate Minerals - Crystallography, Geochemistry and Environmental Significance* 40, pp. 1–112. DOI: 10.2138/rmg.2000.40.1.
- Hurowitz, Joel A., Nicholas J. Tosca, and Darby Dyar (2009). “Acid production by $\text{FeSO}_4 \cdot n\text{H}_2\text{O}$ dissolution and implications for terrestrial and martian aquatic systems”. In: *American Mineralogist* 94.2-3, pp. 409–414. DOI: doi:10.2138/am.2009.3085. URL: <https://doi.org/10.2138/am.2009.3085>.
- Hussmann, H., C. Sotin, and J.I. Lunine (Jan. 2015). “Interiors and Evolution of Icy Satellites”. In: pp. 605–635. DOI: 10.1016/B978-0-444-53802-4.00178-0.
- Jambor, J., Darrell Nordstrom, and Charles Alpers (Jan. 2000). “Metal-sulfate Salts from Sulfide Mineral Oxidation”. In: *Reviews in Mineralogy and Geochemistry* 40, pp. 303–350. DOI: 10.2138/rmg.2000.40.6.
- Klingelhofer, Goestar, R. Morris, Daniel Rodionov, Christian Schröder, A. Yen, D. Ming, and I. Fleischer (Jan. 2006). “Mineralogy on Mars at Gusev Crater and Meridiani Planum as seen by the MER Mössbauer Spectrometers”. In: -1, p. 593.
- Koike, C., H. Mutschke, H. Suto, T. Naoi, H. Chihara, Th. Henning, C. Jäger, A. Tsuchiyama, J. Dorschner, and H. Okuda (Apr. 2006). “Temperature effects on the mid-and far-infrared spectra of olivine particles”. In: 449.2, pp. 583–596. DOI: 10.1051/0004-6361:20053256.
- Krane, Kenneth S. (2012). *Modern physics*. Wiley. ISBN: 9781118061145.
- Lepodise, L. M., J. Horvat, and R. A. Lewis (2013). “Collective librations of water molecules in the crystal lattice of rubidium bromide: experiment and simulation”. In: *Phys. Chem. Chem. Phys.* 15 (46), pp. 20252–20261. DOI: 10.1039/C3CP53667J.
- Ling, Z.C. and Alian Wang (Oct. 2010). “A systematic spectroscopic study of eight hydrous ferric sulfates relevant to Mars”. In: *Icarus* 209.2, pp. 422–433. DOI: 10.1016/j.icarus.2010.05.009.

- Majzlan, J., C. N. Alpers, C. B. Koch, R. B. McCleskey, S. C.B. Myneni, and J. M. Neil (Aug. 2013). “Vibrational, X-Ray Absorption, and Mossbauer Spectra of Sulfate Minerals from the Weathered Massive Sulfide Deposit at Iron Mountain, California”. In: *Chem. Geol* 284:296,2011.
- Markovich, R.J. and C. Pidgeon (1991). “Introduction to Fourier Transform Infrared Spectroscopy and Applications in the Pharmaceutical Sciences”. In: *Pharm Res* (8), pp. 663–675. DOI: 10.1023/A:1015829412658.
- Mauro, Daniela, Cristian Biagioni, Marco Pasero, and Federica Zaccarini (May 2019). “Crystal-chemistry of sulfates from Apuan Alps (Tuscany, Italy). II. Crystal structure and hydrogen bonding system of romerite, $\text{Fe}^{2+}\text{Fe}^{3+}_2(\text{SO}_4)_4(\text{H}_2\text{O})_{14}$ ”. In: *Atti della Societa Toscana di Scienze Naturali* 125, pp. 5–11. DOI: 10.2424/ASTSN.M.2018.19.
- McCord, Thomas B., Gary B. Hansen, Fraser P. Fanale, Robert W. Carlson, Dennis Matson, Torrence V. Johnson, William Smythe, James K. Crowley, P. D. Martin, Adriana C. Ocampo, Charles Hibbitts, and James Charles Granahan (1998). “Salts on Europa’s surface detected by Galileo’s near infrared mapping spectrometer. The NIMS Team.” In: *Science* 280 5367, pp. 1242–5.
- Mitsutake, Hery, Ronei Jesus Poppi, and Márcia Cristina Breitreitz (2019). “Raman Imaging Spectroscopy: History, Fundamentals and Current Scenario of the Technique”. In: *Journal of the Brazilian Chemical Society*.
- Nakamoto, Kazuo (2009). *Infrared and Raman spectra of inorganic and coordination compounds*. Wiley.
- Nesbitt, H. Wayne, G. Michael Bancroft, and Grant S. Henderson (June 2018). “Temperature dependence of Raman shifts and line widths for Q0 and Q2 crystals of silicates, phosphates, and sulfates”. In: *American Mineralogist* 103.6, pp. 966–976.
- Pardo, O.S., V. Dobrosavljevic, T. Perez, W. Sturhahn, Z. Liu, G.R. Rossman, and J.M. Jackson (2022). “X-ray diffraction reveals two structural transitions in szomolnokite, *American Mineralogist*, in press”. In: *American Mineralogist*. (in press).
- Pasquini, Celio (2003). “Near Infrared Spectroscopy: fundamentals, practical aspects and analytical applications”. In: *Journal of the Brazilian Chemical Society* 14, pp. 198–219.
- Perles, Josefina (2020). “Characterisation and Study of Compounds by Single Crystal X-ray Diffraction”. In: *Crystals* 10.10. ISSN: 2073-4352. DOI: 10.3390/cryst10100934.

- Postmus, C., J. R. Ferraro, and S. S. Mitra (Oct. 1968). “Pressure Dependence of Infrared Eigenfrequencies of KCl and KBr”. In: *Phys. Rev.* 174 (3), pp. 983–987. DOI: 10.1103/PhysRev.174.983.
- Richards, Jeremy P. (1998). “Sulfate Minerals”. In: *Geochemistry*. Dordrecht: Springer Netherlands, pp. 603–603. ISBN: 978-1-4020-4496-0. DOI: 10.1007/1-4020-4496-8_302.
- Ross, Nancy and Robert Hazen (Jan. 1989). “Single crystal X-ray diffraction study of MgSiO₃ perovskite from 77 to 400 K”. In: *Physics and Chemistry of Minerals* 16, pp. 415–420. DOI: 10.1007/BF00197010.
- Rothstein, Y., Elizabeth Sklute, M. D. Dyar, and M. Schaefer (Feb. 2005). “Effects of Variable Temperature on Mossbauer Data Acquisition: Laboratory-based and MER A Results”. In.
- Siebert, F. and Peter Hildebrandt (2008). *Vibrational spectroscopy in life science. Tutorials in biophysics*. Wiley-VCH. ISBN: 9783527405060.
- Sobron, Pablo and Alian Wang (2012). “A planetary environment and analysis chamber (PEACH) for coordinated Raman–LIBS–IR measurements under planetary surface environmental conditions”. In: *Journal of Raman Spectroscopy* 43, pp. 212–227.
- Soderlund, Krista M., Klára Kalousová, Jacob Buffo, Christopher R. Glein, Jason C. Goodman, Giuseppe Mitri, G. Wesley Patterson, Frank Postberg, Marc Rovira-Navarro, Tina Rückriemen, Joachim Saur, Britney Elyce Schmidt, Christophe Sotin, Tilman Spohn, Gabriel Tobie, Tim Van Hoolst, Steven Douglas Vance, and Bert L. A. Vermeersen (2020). “Ice-Ocean Exchange Processes in the Jovian and Saturnian Satellites”. In: *Space Science Reviews* 216, pp. 1–57.
- Squyres, S.W., J Grotzinger, Raymond Arvidson, J.F. Bell, Calvin WM, P.R. Christensen, B.C. Clark, J.A. Crisp, William Farrand, K. Herkenhoff, J Johnson, Goestar Klingelhofer, Andrew Knoll, S McLennan, Harry McSween, R Morris, James Rice Jr, R Rieder, and LA Soderblom (Jan. 2005). “In Situ Evidence for an Ancient Aqueous Environment at Meridiani Planum, Mars”. In: *Science (New York, N.Y.)* 306, pp. 1709–14. DOI: 10.1126/science.1104559.
- Stuart, Barbara (2004). *Infrared spectroscopy. [electronic resource] : fundamentals and applications*. Analytical techniques in the sciences. J. Wiley.
- Suryanarayana, C. and M. Grant Norton (1998). *X-Ray Diffraction. [electronic resource] : A Practical Approach*. Springer US. ISBN: 9781489901484.

- Talla, Dominik and Manfred Wildner (Dec. 2019). “Investigation of the kieserite – szomolnokite solid-solution series, $(\text{Mg,Fe})\text{SO}_4 \cdot \text{H}_2\text{O}$, with relevance to Mars: Crystal chemistry, FTIR, and Raman spectroscopy under ambient and martian temperature conditions”. In: *American Mineralogist* 104, pp. 1732–1749. DOI: 10.2138/am-2019-6983.
- Theophanides, Theophile(Theo) (Apr. 2012). “Introduction to Infrared Spectroscopy”. In: ISBN: 978-953-51-0537-4. DOI: 10.5772/49106.
- Vandenabeele, Peter (2013). *Practical Raman spectroscopy. [electronic resource] : an introduction*. Wiley.
- Vandenbergh, R.E., E. de Grave, and P.M.A. de Bakker (1994). “On the methodology of the analysis of Mössbauer spectra”. In: *Hyperfine Interactions* 83.1, pp. 29–49. DOI: 10.1007/BF02074257.
- VanLoan, P. R. and E. W. Nuffield (1959). “An x-ray study of roemerite”. In: *Canadian Mineralogist* 6, pp. 348–356.
- Volkov, Dmitry S., Olga B. Rogova, and Mikhail A. Proskurnin (2021). “Temperature Dependences of IR Spectra of Humic Substances of Brown Coal”. In: *Agronomy* 11.9. ISSN: 2073-4395. DOI: 10.3390/agronomy11091822.
- Waseda, Yoshio, Eiichiro Matsubara, and Kozo Shinoda (2011). *X-Ray Diffraction Crystallography. [electronic resource] : Introduction, Examples and Solved Problems*. Springer Berlin Heidelberg. ISBN: 9783642166358.
- Westland, Robin E. (Aug. 2012). “New phases in the hydrous sulfate system, a supporting argument that the mineral lausenite is a formula $\text{Fe}_2(\text{SO}_4)_3 \cdot 5 \text{H}_2\text{O}$ and the crystal structure refinement and hydrogen bonding scheme of the minerals quenstedtite and roemerite”. MA thesis.
- Wolfe, C. W. (May 1937). “Re-orientation of römerite”. In: *American Mineralogist* 22.5, pp. 736–741. ISSN: 0003-004X.
- Yen, A., R. Morris, B. Clark, R. Gellert, A. Knudson, S. Squyres, David Mittlefehldt, D. Ming, Raymond Arvidson, T. McCoy, Mariek Schmidt, and J. Hurowitz (June 2008). “Hydrothermal processes at Gusev Crater: An evaluation of Paso Robles class soils”. In: *Journal of Geophysical Research* 113. DOI: 10.1029/2007JE002978.
- Yoshida, Yutaka and Guido Langouche (2013). *Mössbauer Spectroscopy. [electronic resource] : Tutorial Book*. Springer Berlin Heidelberg. ISBN: 9783642322204.